

Answers to

Interactive comment on “Microwave and submillimeter wave scattering of oriented ice particles” by Manfred Brath et al.
Anonymous Referee #1

February 4, 2020

General comments

Reviewer: This article by Brath et al. presents a novel, highly valuable study and database of the properties of oriented snow particles in the atmosphere at low to high microwave frequencies. This has been a goal of the local research community for years, and the reviewer is rather glad that he came across it for review.

The resulting database is gigantic, and the complexities of assembling this database are discussed at length throughout the manuscript. Great care was taken to describe all of the conventions and equations involved in the scattering calculations, particle rotations and subsequent radiative transfer simulations. The reviewer congratulates the authors on this achievement.

It is quite possible, however, for readers to become lost in this level of detail and lose the main thrust of the paper. Also, earlier sections of the manuscript (e.g. pp. 3 and 10) refer the reader to details in section 4 (p. 11). As such, the reviewer suggests that the authors attempt to simplify by moving some of these details into appendices and somewhat reordering the manuscript. There are also many small points (both scientific and formatting) that should be addressed. The overall recommendation is to revise and resubmit.

Answer: As suggested, we shifted the details of section 4 to the Appendix. Furthermore, we revised the paper considering the comments of all three reviewers.

Section-by-section comments

Abstract

Reviewer: The abstract is too vague. It states that you performed simulations and made a database for use with the upcoming Ice Cloud Imager. Your summary section contains information that should be emphasized here. Results from Sections 6 and

7 can further provide examples of why undertaking the construction of this database was worthwhile.

Answer: We revised accordingly.

Reviewer: - Line 7: "The additional tilt angle adds an additional dimension" -> . . . adds an additional degree of freedom. Dimension can be rather confusing in the context of this paper.

Answer: We changed it. We now write: "The additional tilt angle further increases the complexity."

Reviewer: - Line 8: dipol -> dipole

Answer: Changed as suggested.

Reviewer: - Line 9: Perhaps mention that these habits were first introduced in a previous paper. Mention that the database covers multiple temperatures.

Answer: We now mention that the database covers multiple temperatures.

Reviewer: - Line 10: The data is -> The data are

Answer: We change it.

Introduction:

Reviewer: You need information on why polarized scattering properties are important. What new information content would they provide for data assimilation / forecasting? Metop-SG-B's ICI instrument (launching in the early 2020s) will need better models of snow particle scattering to properly retrieve ice cloud properties. To provide for this, you need a few key components: accurate ice particle shapes, a polarized radiative transfer model, accurate orientation distributions, and polarization-sensitive dataset of ice particle scattering. Eriksson et al. (2018) provides the shapes, ARTS provides the radiation model, you assume the orientation distributions and generate the scattering dataset that studies / people / instruments can use.

Answer: We revised the introduction according to that. We now state, why polarization is important and why it is important to have scattering properties of oriented and realistically shaped particles. Furthermore, we rephrased the goal of the study and the idea behind the database.

Reviewer: - Line 15: “channels of these passive” -> “channels of passive”

Answer: Changed as suggested.

Reviewer: - Lines 17 and elsewhere: “Currently, . . . GPM and MADRAS . . . are the only spaceborne microwave radiometer that measure polarization at ice cloud frequencies. GPM and MADRAS observe polarization around 160 GHz.” MADRAS was declared non-operational about two years after launch, and it is no longer collecting scientifically valid data. The sentence should reflect that.

Answer: We corrected that and mention now that due to mechanical failure MADRAS measured only till January 2013.

Reviewer: - Line 19: You might want to discuss the abundance of polarized data available at around 90 GHz. Polarized measurements are also available on Metop-C and on GCOM-W1, but are strongly affected by surface contamination.

Answer: We added some sentences about it. We now mention that there are polarized observations below 100 GHz. We further added that due to the low frequency, the sensitivity considering ice clouds is low (Buehler et al., 2007), though there still can be enough sensitivity for precipitating ice, and that at these frequencies surface contamination is an issue.

Reviewer: - Line 22: The mentioning of particle orientations is rather abrupt. You need a few expository sentences here.

Answer: Done as suggested. We restructured the introduction and gave some additional background considering polarization, see also answer to your first introduction comment.

Reviewer: - Line 24: “realistically shape” -> “realistically shaped”

Answer: Changed as suggested.

Reviewer: - Line 24: “that also possess an orientation” – This dangles from the end of the sentence, and should be rephrased.

Answer: Removed, due to restructuring of the introduction.

Reviewer: - Line 28: “one orientations” -> “one orientation”

Answer: Changed as suggested.

Particle orientation:

Reviewer: This section can get rather technical, and so it is important for the reader to be guided through possible misunderstandings.

- Lines 49 and elsewhere: “spherical symmetry” is a bit confusing, and you seem to be using two competing meanings of this term throughout the manuscript. Consider a symmetric 6-bullet rosette. In Appendix A, line 592, spherical symmetry occurs when $l_{xx} = l_{yy} = l_{zz}$. Contrast to line 49: “If the particle possesses spherical symmetry there is no particle orientation, because it does not matter from which side the particle with spherical symmetry is viewed or how it is rotated – it will always look the same.”: This seems more like radial symmetry.

Answer: According to the American Meteorological Society Glossary of Meteorology radial symmetry and spherical symmetry is the same in three dimensions. “Radial symmetry in two dimensions is often called circular symmetry; in three dimensions, spherical symmetry.” http://glossary.ametsoc.org/wiki/Radial_symmetry Therefore, we did not change it.

Reviewer: - Line 50: Last sentence of paragraph is cumbersome. How about “The particles considered in this paper are not radially symmetric and may be oriented.”?

Answer: We changed it to “The particles considered in this paper are not spherically symmetric and therefore can be oriented.”

Reviewer: - Lines 52-62: “In general, the orientation of a particle in a three dimensional space can be described by a set of three parameters. The three Euler angles are one such parameter set.” - You need to assert in this section that your choice of rotation angles are not necessarily the same rotation angles used elsewhere. There are six pure Euler angle schemes (intrinsic rotations), six Tait-Bryan conventions (extrinsic rotations; some literature sources also consider these to be Euler angles), and several mixed approaches.

Answer: We now state that there is no unique set of parameters and that there are different sets of them depending on the definition of the rotation axes.

Reviewer: - Line 52: “three dimensional” -> “three-dimensional”

Answer: Changed as suggested.

Reviewer: - Lines 56,57 and in many places elsewhere: Something went wrong with the PDF rendering of some of the symbols used in your manuscript (e.g. zyz' notation is displayed as $z[\text{box}]z'$). This happens on different machines (macs, Windows) and using different PDF readers.

Answer: Unfortunately, there were some problems with the font. This happened when the manuscript was uploaded to AMT. We are aware of this.

Reviewer: - Line 62: “important to know” -> “important to note”

Answer: Changed as suggested.

Reviewer: - Line 63: “Additionally to the Euler angles” -> “In addition to the Euler angles”

Answer: Changed as suggested.

Reviewer: - Line 66: You are considering only generally oblate particles (and your particle model is discussed later in the paper). You mention plates here, but it is good to explicitly state that you assume only oblate shapes. If you have something more prolate-shaped (i.e. columns), then its general alignment to vertical or horizontal becomes a very complicated function of drag and other local conditions (you can get preferential vertical instead of horizontal alignment).

Answer: We revised that part and now discuss the validity of our assumption.

Reviewer: - Lines 80, 81 and 98: Define the abbreviations (TRO, ARO) in lines 80,81 instead of in a subsequent figure caption (line 98).

Answer: Done as suggested.

Reviewer: - Line 90: Total scattering angle is a function of the angle between incoming and outgoing direction, and it might be useful to include the equation here.

Answer: Done as suggested.

Reviewer: - Lines 94+, and 70-79: You seem to be aligning your ensemble of particles in the same way, regardless of the different moments of inertia, sizes and aspect ratios of the particles. Why not allow for different particles in your ensemble to have different preferential alignments, perhaps using von Mises-Fisher or Fisher-Bingham-Kent distributions? It’s worth discussing, especially since related work has been presented by the GPM team. This also relates to my comment in section 5 – can the raw (per-orientation) data be made available for users to manipulate independently?

Answer: Considering your comment and after reading the specific lines again, the lines 70 - 79 may be misleading, because it was not stated clearly in manuscript what is the basic idea behind the database and its usage, which we now do. Our main assumption is that there is no preferred orientation of the particles in azimuth direction. Based on that we want the users to decide, which tilt angle β (zenith orientation) or tilt angle distribution they need. That is why we calculate the scattering properties for several tilt angles β for all particle sizes and shapes.

In the revised introductions, we now state: "The idea behind the scattering database is that the users can use scattering data of a desired zenith orientation or combine the data of different zenith orientations to mimic any desired distribution of zenith orientations." We also rephrased the goal of the study, see answers to section-by-section comments for introduction.

Reviewer: - Lines 100-116: The paragraph is wordy and would be hard to understand for someone outside of the immediate field. Lines 101 and 111 state, "to get a better picture of it" and "to get a better idea of it". You might need to add in a descriptive figure here.

Answer: Done as suggested.

Basic setup and shape data

Reviewer: This section reads well.

- Line 118: Amsterdam DDA's name was changed. See a recent version of the manual for their rationale.

Answer: Changed as suggested.

Reviewer: - Lines 125-126: As described elsewhere in the manuscript, the two hydrometeor habits have multiple shapes in each habit. The text here is somewhat misleading and should be rephrased. Or, prefix with the sentences in lines 127-128.

Answer: We reordered it as suggested and further revised that section considering your and the other reviewers' comments.

Reviewer: - Line 134: Volume equivalent diameter should be defined. It has multiple meanings in the field, and I am assuming that you mean the diameter of an equal-volume sphere made of solid ice, later used in line 310.

Answer: We added the definition of the volume equivalent diameter to the text. The volume equivalent diameter is defined as the diameter of a solid ice sphere with the same mass as the particle.

Reviewer: - Line 134: Same with maximum diameter. Assuming you mean in three dimensions.

Answer: We added the definition of the maximum diameter to the text. The maximum diameter is defined as the diameter of the minimum circumscribed sphere of a particle.

Reviewer: - Line 135: Why are the sizes slightly different?

Answer: The plate type 1 habit in our study has slightly different sizes than the plate type 1 in Eriksson et al. (2018), because an older version of shape data was used than in Eriksson et al. (2018) and given the high computational costs of the scattering calculation a recalculation was not feasible. We added previous sentence to the text.

Reviewer: - Line 142: Why are the frequencies slightly different?

Answer: Due to a rounding mistake when the simulation was set up, the frequencies of the plate type 1 habit slightly deviate from the frequencies of the large plate aggregate habit by at maximum 0.5 GHz. We added previous sentence to the text.

Reviewer: - Page 7: 886 GHz is quite high! What interdipole spacing did you use when calculating these results?

Answer: For all particles considered in our study holds

$$|m|kd < \frac{1}{2} \quad (1)$$

with m the refractive index of ice, k the wavelength and d the dipole size. With the microwave refractive index of ice this result in roughly 22 dipoles per wavelength. Furthermore, all simulated particles consist of at least 1,000 dipoles so that small particles are reasonable resolved. We added a similar statement to Section Basic setup and shape data.

Reviewer: - Line 158: Spacing. "Fig. 4 b" -> "Fig. 4b" to match "Fig. 4a" on line 156.

Answer: Changed so that they now match.

Reviewer: - Line 158: "This approach is analogue to the analytic T-matrix method, only in a much more numerical way." I am uncertain if many readers will appreciate the analogy.

Answer: We removed it.

Reviewer: - Line 168: “stokes” -> “Stokes”

Answer: Changed as suggested.

Reviewer: - Line 195: The number of incidence angles seems to be rather low. The reviewer recognizes that adding more would be prohibitively expensive, and that the manuscript is already a substantial improvement on what was available before. However, it might be worth commenting on in the text.

Answer: We agree that it can seem to be, but the number of incidence angles is not low. Unfortunately, we forgot to mention in the text what accuracy we aim for the database. We now state in Section Basic setup and shape data that we aim for an accuracy of the scattering database in the order of a few percent. Relative to this, the number of incidence angles is sufficient. We further added some sentences considering the number of incidence angles.

Reviewer: - Line 202: “appendix” -> “Appendix”

Answer: Changed as suggested.

Reviewer: - Section 4.1: Particle rotation: No comments here.
- Lines 252, 253, 256: “stokes” -> “Stokes”

Answer: Changed as suggested.

Results of the scattering simulations

Reviewer: There were 69 particles overall, and 7245 cases, with over a million core hours, and about 1.5 TB or raw data. However, are users of the database are restricted to the orientationally-averaged set? The summary section, line 517, implies that only the summarized data are available.

Answer: Yes, only the averaged data is publicly available, because it is not feasible for us to host the non-averaged data, but the data can be given to anyone who is interested by contacting us. We added a similar statement to the text.

Reviewer: - Line 290: spacing. “scattering matrix Zaroand” -> “Zaro and”

Answer: Changed as suggested.

Reviewer: - Eqn 33: there is a spurious dot between the two lines of the equation. Was this supposed to be a comma?

Answer: We corrected it.

Reviewer: - Line 295: Wrong font for absorption vector “a”.

Answer: We corrected it.

Reviewer: - Line 307: “3” -> “three”

Answer: Changed as suggested.

Reviewer: - Lines 337-350, 375, Fig. 8,9 captions: PDF rendering problem with the asymmetry parameter.

Answer: We corrected it, see answers to section-by-section Particle orientation.

Reviewer: - Line 361: “Eqn.” -> “Eq.” to match how you abbreviate everywhere else.

Answer: Changed as suggested.

Radiative transfer simulations

Reviewer: No major comments.

- Line 456: “addionally” -> “additionally”

Answer: Changed as suggested.

Reviewer: - Line 487: “sphere like” -> “sphere-like”

Answer: Changed as suggested.

Summary

Reviewer: Good section overall. Some of the information here should be highlighted in the abstract.

Answer: Done as suggested.

Reviewer: - Line 552: fix opening quote before Climate

Answer: Done as suggested.

Appendices

Reviewer: No major comments.

- Lines 569, 577, 614, 616, 617: fix rendering

Answer: We corrected it, see answers to section-by-section Particle orientation.

Reviewer: - Line 592: See comment in Particle Orientation section.

Answer: See first answer in answers to section-by-section Particle orientation.

References

Reviewer: Various formatting typos.

- Line 666: "in: 2016" -> "in 2016"?

Answer: No, it is correct as it is. It is the official citation from IEEE.

Reviewer: - Line 670: "157?GHz"

Answer: Corrected it.

Reviewer: - Line 700: "Iet"?

Answer: Changed to "IET".

Reviewer: - Lines 701-704: Title capitalization is inconsistent with other references.

Answer: Corrected it.

Reviewer: - Line 706: Cambridge University Press (capitalization)

Answer: Corrected it.

Reviewer: - Line 726: "ADDA: Capabilities". Capitalization in contrast to line 662.

Answer: Corrected it.

References

- Buehler, S. A., Jiménez, C., Evans, K. F., Eriksson, P., Rydberg, B., Heymsfield, A. J., Stubenrauch, C. J., Lohmann, U., Emde, C., John, V. O., and et al.: A concept for a satellite mission to measure cloud ice water path, ice particle size, and cloud altitude, *Quarterly Journal of the Royal Meteorological Society*, 133, 109–128, <https://doi.org/10.1002/qj.143>, 2007.
- Eriksson, P., Ekelund, R., Mendrok, J., Brath, M., Lemke, O., and Buehler, S. A.: A general database of hydrometeor single scattering properties at microwave and sub-millimetre wavelengths, *Earth System Science Data*, 10, 1301–1326, <https://doi.org/10.5194/essd-10-1301-2018>, URL <https://www.earth-syst-sci-data.net/10/1301/2018/>, 2018.

Answers to

Interactive comment on “Microwave and submillimeter wave scattering of oriented ice particles” by Manfred Brath et al.
Anonymous Referee #2

January 31, 2020

Reviewer: The manuscript "Microwave and submillimeter wave scattering of oriented ice particles" is well-written, logically constructed, and highly impactful. Databases of such oriented particles, particularly with complete phase and extinction matrix information, are not available, so this dataset is expected to be groundbreaking for microwave, millimeterwave, and submillimeter-wave sensor modeling applications. The radiative transfer results are very encouraging, and show that the authors have done a good job of creating a useful dataset. After addressing some minor clarifying issues, this manuscript is ready for publication.

My biggest concern is the precision to which these calculations have been run (see lines 176-178; 283-285). I understand that these are computationally-expensive calculations, so improving on these numbers is beyond the scope of this paper. However, the cross-polarization terms, i.e., Z_{12} and Z_{21} , are orders of magnitude smaller than Z_{11} , so these terms may be unreliable, and looking at the processed data, there seems to be a lot of noise that is of the same order of magnitude as the signal. Luckily these terms are small, and the largest expected contribution would be to radar polarimetric variables, especially LDR. I think the authors should make a note of this when discussing the precision relative to Z_{11} (and the other phase matrix terms).

Answer: We have to admit that we forgot to address the accuracy of the database within the text. In the revised version, we do. Due to the high demands in view of computation time and the amount of data, we had to compromise in terms of the accuracy of the resulting scattering data, which we forgot to mention. Considering the measurement errors of existing and upcoming passive MW and SubMM sensors, which are in the order of $\mathcal{O}(1\text{ K})$, and the brightness temperature depression due to scattering of frozen hydrometeors, which is typically $< 100\text{ K}$, we aim for an accuracy of the scattering database in the order of a few percent. We added a similar statement to the Section Basic setup and shape data and added it to the summary to clearly address this. Furthermore, we now relate the truncation of the spherical harmonics in Section Scattering calculations to the desired accuracy.

Reviewer: The authors should make clear that the amplitude scattering matrix (equation 11) operates on the complex electric field terms.

Answer: We added that the scattering amplitude matrix is a complex matrix and that it operates on the electric field, whereas the extinction, the scattering, and the Mueller matrix operate on the Stokes vector, which is a real vector.

Reviewer: The authors should explicitly state that orientational averaging must be done incoherently, that is at the the Mueller (or Phase) matrix stage, due to the power terms in the top left block of the Phase matrix.

Answer: We added to Eq. 2 and 3 a statement that we assume independent scattering and that therefore we assume incoherent scattering.

Reviewer: When discussing mirror partners and mirror symmetry, please cite van de Hulst (1957) and Mishchenko (2002). There is a really nice explanation with stick figures in both publications.

Answer: Done as suggested.

Reviewer: Also in reference to mirror particles, for the RT simulations in section 6.1, were the particles averaged with their mirror partners (with respect to the incidence plane)? This is important for properly conditioning the Z12 and Z21 Phase matrix parameters for the target medium of preferential alignment with zero mean canting angle.

Answer: No averaging of the scattering data of the particles with its mirrored version was done for the radiative transfer simulation. Due to the orientational averaging and the random structure of the large plate aggregate the effect of the non-mirror symmetry are so small, that we neglected it for the radiative transfer simulations. Particles like the plate type 1 automatically fulfill this, as they are mirrorsymmetric. We added a similar statement to the text addressing this.

Technical corrections:

Reviewer: There are minor typos throughout the manuscript that need to be fixed, but the document as a whole is very clear.

Answer: Corrected them.

Reviewer: There are a few symbols that did not render properly, one of which was the asymmetry parameter.

Answer: Unfortunately, there were some problems with the font. This happened when the manuscript was uploaded to AMT. We are aware of this.

Answers to

Interactive comment on “Microwave and submillimeter wave scattering of oriented ice particles” by Manfred Brath et al.
Davide Ori (dori@uni-koeln.de)

January 31, 2020

Reviewer: The paper presents an important step forward in the currently available scattering databases of snow particles at microwave frequencies by assuming the possibility of ice particles with preferential orientations. This is an important contribution which I recommend for publication, but I would also like to list some comments aiming to improve the value of the paper.

1. The orientation averaging technique lacks some validation. A very basic sanity check would be to calculate the integral over $\cos(\beta)$ at the various θ_{inc} and compare with the previously published database (DB) for total random orientation (TRO). Another useful plot to include would be the convergence of the integral with respect to the number of points of the icosahedral grid. At line 195 it is stated that a variable number of points is used (between 162 and 2562), perhaps these convergence plots would clarify why, sometimes, a smaller number of orientation samples is sufficient.

Answer: You are right this is missing. We forgot to mention it in the text. We tested our method by simulating the scattering of azimuthally randomly oriented prolate ellipsoids and compared the results against T-matrix calculations. The overall differences in view of the extinction matrix and the scattering matrix were in the order of a few percent. We added a similar statement to the text. Considering line 195, we revised it. We now explain, why sometimes, a smaller number of orientations are sufficient.

Reviewer: 2. The averaging scheme is presented as a solution to various challenges that sequentially appear in the text. It is hard, sometimes, to follow this approach because it requires to rethink about the setup many times without a clear final goal to aim to. I want to suggest to introduce the three main reference frames of the problem from the beginning: these are the laboratory (satellite) reference frame, the particle reference frame, and the wave reference frame. By doing so, one can state from the beginning that the scope is to have the polarized scattering properties defined with respect to the satellite reference frame and some transformations are needed because for scattering calculations the wave reference frame is a more natural

option used in scattering codes. Also what is called the orientation of the non-rotated particle is nothing less than the particle reference frame.

Answer: We agree that it is sometimes hard to follow. We revised that part considering on your suggestion.

Reviewer: 3. Line 62. This phrase, somehow implies that there is a special subset of rotation matrices that are orthogonal and no couple of rotation matrices are commutative with respect to multiplication. I think all rotation matrices are orthogonal and some rotation matrices do commute (the ones around the same axis).

Answer: We rephrased the sentence to: “ It is important to note that in general the order of the rotations must not be changed, because the combination of rotations is generally not commutative.”

Reviewer: 4. Line 87. For TRO $p(\beta)$ should be $\frac{1}{2}$ and β should be uniformly distributed in terms of $\cos(\beta)$. Otherwise, the integral does not compute to 1 when $K=1$

Answer: We corrected it. We now define $p(\beta)$ according to Mishchenko and Yurkin (2017) Eq. 4. This means

$$p(\beta) = \frac{\sin \beta}{2}. \quad (1)$$

Due to that we adjusted all equations in the text that involve averaging over the tilt angle β (Eq. 2,3, and 37).

Reviewer: 5. Line 110. I think here the non-symmetry is respect to the scattered azimuth, not the incident which is actually irrelevant for Zaro.

Answer: We removed “to incidence azimuth direction” from that specific sentence.

Reviewer: 6. Line 121. ADDA can actually also compute scattering properties for distributions of angles through input files, this includes azimuthally averaging. The reason why this is not used in the study is that this approach involves the solution of the computationally demanding DDA problem for slightly different orientations many times (for the different combinations of tilt angle and wave incidence).

Answer: We rephrased it. We now state that the internal averaging method of ADDA is not suitable for our approach.

Reviewer: 7. Line 130. D_0 should have explicit units, which I assume are μm .

Answer: We added the unit.

Reviewer: 8. Line 179-182. I do not see why a regular grid is advantageous for resolving the for/back-ward scattering peaks. A regular grid means that the azimuth and polar angles are equally spaced. The points at the same polar angle are getting closer in azimuth distance as the polar angle approaches the poles. The scattering peaks mean that there is a high variability of the scattering intensity with respect to the polar angle and thus would demand an increased resolution in polar angles. The polar angle resolution is always the same here.

Answer: We removed that sentence.

Reviewer: 9. Lines 209-214. In my opinion, two points are missing in the list of steps: first is the projection over spherical harmonics of the scattered fields. And the second is the barycentric interpolation of the gridded data. The second is important because it clarifies that the computed properties for a certain β and θ_i are actually coming from slightly different angles.

Answer: We agree that the projection on spherical harmonics was missing in that list especially due to the truncation of them to reduce the amount of data. Therefore, we added it. We do not think that the barycentric interpolation is missing, because we think it is part of the averaging operation as the Gauss-Legendre quadrature is part of the averaging operation. Furthermore, the interpolation is explicitly stated in the paragraph before the list of steps. Therefore, we did not add it to the list.

Reviewer: 10. Line 220. The three rotation matrices are different. Perhaps a better notation would be $R_{\alpha\beta\gamma} = R_{\alpha}(\alpha) R_{\beta}(\beta) R_{\gamma}(\gamma)$

Answer: Changed as suggested

Reviewer: 11. Line 284. What is called accuracy $\epsilon = 1\%$ I think is the internal stopping criterion for the ADDA iterative solver and should not be confused with the accuracy of the calculations which is hard to evaluate and yet not clearly understood. Perhaps the authors should include in the supplementary material, for just one particle and one orientation what is the effect on the scattering properties (just plot phase functions) of this choice of ϵ with respect to the default value of 10^{-5} (three orders of magnitude smaller!).

Answer: You are right. We revised that part. We now say explicitly that it is the internal stopping criterion. Furthermore, we state that we aim for an accuracy of a few percent for our database. Therefore, setting the stopping criterion to 10^{-2} is a compromise in terms of accuracy due to the high demands in view of computation time and the amount of data.

Considering the measurement errors of existing and upcoming passive MW and SubMM sensors, which are in the order of $\mathcal{O}(1\text{K})$, and the brightness temperature depression due to scattering of frozen hydrometeors, which is typically $< 100\text{K}$, an accuracy of the scattering database in the order of a few percent seems sufficient.

Reviewer: 12. Line 381. In the figure, I see $\beta = 0, 50, 90$ but in the text, $\beta = 30$ is mentioned, perhaps there is a typo?

Answer: Yes, that were typos.

Reviewer: 13. Line 397-402. Here the authors state that the database is not optimized for radar calculations because the spherical harmonics projection is not good at forward and backward scattering. Perhaps the authors should better describe what they meant at line 177 with RMSE of less than 0.5% due to the spherical harmonics. 0.5% is actually quite insignificant for radar applications. Also this problem can be immediately solved by making available the original DDA computations at single orientations, perhaps by request to the corresponding author. I think this last piece would also make the paper fully compliant with the Copernicus open-data policy.

Answer: Considering line 177, we revised that. We now relate the truncation of the spherical harmonics in Section Scattering calculations to the desired accuracy. We have to admit, that due to the missing statements on the desired accuracy of the database, it was not clear why we used an RMSE of 0.5%.

We cannot make the original DDA computations available. We could not store them permanently, because the data was too big. But we can make the truncated data from DDA computations available upon request. We added a statement considering the data availability to the text.

Reviewer: 14. The scattering properties of hexagonal crystals are symmetric with respect to θ_i due to the planar symmetry of the particles. This is not true for aggregates that are not symmetric. The authors have oriented the aggregates according to their principal axis of inertia. This is, in general, a good fast approach, but it introduces an arbitrary decision about what is the direction of the main (vertical) axis of inertia. In my opinion, there is no clear criterion to decide whether this axis should look up or down. As a consequence, one could argue that the scattering properties for $\theta_i = \lambda$ should be averaged with those for $\theta_i = 180 - \lambda$ giving planar symmetry also to the aggregates and reducing the storage footprint of the database.

Answer: You are correct. When using the axis of inertia there is no unique criterion to decide whether the axis should be upward or downward. Therefore, we use an additional criterion, see Appendix Initial particle alignment step 4. We define, if the center of the circumscribed sphere of the particle is found to be below the mass-center of the particle (with

respect to the z-axis), then the particle is said to be aligned upright and vice versa. We did not consider your suggested averaging, because we want the users to decide what they want or need.

Reviewer: 15. Equations (20) and (21) show how to rotate the polarization vectors of the Mueller matrix. I wonder if this is done before the barycentric interpolation. In my view, the scattering properties of the three vertexes should be first aligned with the direction and polarization of point D. If the forward/backward scattering direction lies within the triangle ABC this can cause quite dramatic cancellation due to the flipping of the polarization direction among the points A, B, and C.

Answer: We think we do not fully understand your point. Equations (20) and (21) describe how the Mueller matrix and the extinction matrix are transformed. The interpolation is done with respect to the incidence direction not with respect to the scattering directions. Actually, the points (vertices) of the triangle are the three nearest sample points to our desired incidence direction at point D after the rotation of the particle system. The sample points are the set of the incidence directions at which we have calculated the Mueller matrix with ADDA. At each of the three nearest sample points we transform the polarization according to Eq. 22 using the Stokes matrices. And after that we do the interpolation, which is essentially a weighted averaged of the Mueller matrices of these three sample points.

References

Mishchenko, M. I. and Yurkin, M. A.: On the concept of random orientation in far-field electromagnetic scattering by nonspherical particles, *Optics letters*, 42, 494–497, 2017.

Microwave and submillimeter wave scattering of oriented ice particles

Manfred Brath¹, Robin Ekelund², Patrick Eriksson², Oliver Lemke¹, and Stefan A. Buehler¹

¹Universität Hamburg, Faculty of Mathematics, Informatics and Natural Sciences, Department of Earth Sciences, Meteorological Institute, Hamburg, Germany

²Department of Space, Earth and Environment, Chalmers University of Technology, Gothenburg, Sweden

Correspondence: Manfred Brath
(manfred.brath@uni-hamburg.de)

Abstract. Microwave (1 GHz–300 GHz) dual-polarization measurements above 100 GHz–100 GHz are so far sparse, but they consistently show ~~that larger ice hydrometeors tend to deviate from the standard assumption of polarized scattering signals of ice clouds. Existing scattering databases of realistically shaped ice crystals for microwave and submillimeter (> 300 GHz) typically assume~~ total random orientation. ~~This conclusion has been derived by conceptual models, while the first detailed~~ 5 ~~simulations, recreating the observed polarization patterns, are presented in this study. The ice particles are assumed to be,~~ which cannot explain the polarized signals. Conceptual models show that the polarization signals are caused by oriented ice particles. Only few works considering oriented ice crystals exist, but they considered microwaves only. Assuming azimuthally randomly oriented ice particles with a fixed but arbitrary tilt angle. ~~The,~~ we produced scattering data for azimuthal random orientation is much more complex than for total random orientation two particle habits (51 hexagonal plates and 18 10 plate aggregates), 35 frequencies between 1 GHz and 864 GHz, and 3 temperatures (190 K, 230 K, 270 K). The scattering data of azimuthally randomly oriented particles depends in general on the incidence angle and two scattering angles compared to one angle scattering for total random orientation. The additional tilt angle adds an additional dimension further increases the complexity. The simulations are based on the discrete dipole-dipole approximation in combination with a self-developed self-developed orientation averaging approach. ~~Data for two particle habits (51 hexagonal plates and 18 plate aggregates)~~ 15 ~~and 35 frequencies between 1 GHz and 864 GHz were produced. The~~ The scattering data is publicly available from Zenodo (<https://doi.org/10.5281/zenodo.3463003>). This effort is also an essential part of preparing for the upcoming Ice Cloud Imager (ICI) that will perform polarized observations at 243 GHz and 664 GHz, ~~which will deliver new insights about clouds. Using~~ our scattering data radiative transfer simulations with two liquid hydrometeor species and four frozen hydrometeor species of polarized GMI (GPM (Global Precipitation Measurement) Microwave Imager) observations at 166 GHz were conducted. 20 The simulations recreate the observed polarization patterns. For slightly fluttering snow and ice particles, the simulations show polarization differences up to 11 K using plate aggregates for snow, hexagonal plates for cloud ice and totally randomly oriented particles for the remaining species. Simulations using strongly fluttering hexagonal plates for snow and ice show similar polarization signals. Orientation, shape and the hydrometeor composition affect the polarization. Ignoring orientation can cause a negative bias for vertically polarized observations and a positive bias for horizontally polarized observations.

25 1 Introduction

Passive microwave (MW) observations are nowadays a standard tool for cloud observation. The ice cloud related sounding channels of ~~these~~ passive microwave sensors typically do not possess a fixed polarization or they measure only at one polarization. Observation of polarization in view of MW and submillimeter (SubMM) remote sensing of ice clouds is still rare. Existing passive microwave sensors that measure polarization are typically confined to frequencies below 100GHz. Due to the
30 low frequency, their sensitivity considering ice clouds is low (Buehler et al., 2007), though there still can be enough sensitivity for precipitating ice, but these sensors are affected by surface contamination.

Currently, GMI (GPM (Global Precipitation Measurement) Microwave Imager, Hou et al., 2013) ~~and is the only spaceborne microwave radiometer that measures polarization above 100GHz. In the past, MADRAS (Microwave Analysis and Detection of Rain and Atmospheric Structure, Defer et al., 2014) are the only spaceborne microwave radiometer that measure on board of~~
35 Megha-Tropique also observed polarization at ice cloud related frequencies, but due to mechanical failure only till January 2013 (Shivakumar and Pircher, 2013). GMI and MADRAS observe polarization around 160GHz. ~~With the upcoming ICI (Ice Cloud Imager, Bergad et al. (2016); Buehler et al. (2012, 2007)) there will be polarized observations at 243GHz and at 664GHz. These polarized observations will deliver new insights about clouds and their structure, because the assumption of totally randomly oriented particles cannot explain the strong polarization signals found in Defer et al. (2014); Gong and Wu (2017); Zeng et al. (20~~
40 ~~To understand these signals we need the scattering properties of realistically shape ice crystals that also possess an orientation.~~

Defer et al. (2014); Gong and Wu (2017) and Zeng et al. (2019) showed MW observations of polarized scattering signals of clouds using GMI and MADRAS. Based on radiative transfer simulations, Defer et al. (2014) and Gong and Wu (2017) explained these polarized signals ~~in conceptually using very simplified assumptions on shape and orientations. In reality, ice by the~~
45 asphericity and a preferred orientation of the ice particles. Therefore, exploiting polarization can deliver additional information about the shape and orientation. Ice crystals have several shapes and sizes in reality. Furthermore, even the cases that have been explained by horizontally aligned particles consist in reality not only of particles with only one ~~orientationsorientation,~~
~~but of particles with several different orientations, from which some orientations may have a higher probability than other orientationsothers.~~ With the upcoming ICI (Ice Cloud Imager, Eriksson et al. (2020); Bergad et al. (2016); Buehler et al. (2012, 2007))
50 there will be additional polarized observations at 243GHz and at 664GHz. These polarized observations will deliver new insights about clouds and their structure, because of their higher sensitivity to ice clouds compared to GMI. The scattering data directly affects simulations and inversions of MW and SubMM ice cloud observations, because the scattering data describes the interaction between ice particles and the electromagnetic radiation. This limits the phenomena that can be considered and the amount of information that can be retrieved from the observations, respectively. Therefore, to exploit polarization, we need
55 the scattering properties of oriented and realistically shaped particles.

Existing single scattering databases of ~~frozen hydrometeors at realistically shaped ice particles for the~~ microwave and submillimeter range, like the ones of Eriksson et al. (2018), Liu (2008) or Hong et al. (2009), assume total random orientation of the scatterers, ~~which~~. This is often a reasonable assumption, but cannot explain polarized cloud signals. This requires oriented

scatterers. The studies of Lu et al. (2016) and of Adams and Bettenhausen (2012) take orientation into account but are limited to frequencies below 94 GHz and 166 GHz, respectively.

~~The aim of this paper is~~ This paper aims to simulate the MW and SubMM scattering properties data of realistically shaped ice crystals that ~~are randomly oriented in azimuth but possess a fixed arbitrary tilt angle relative to zenith~~ possess arbitrary fixed orientations relative to the zenith direction under the assumption that there is no preferred orientation in azimuth direction. The resulting single scattering database is publicly available from Zenodo (<https://doi.org/10.5281/zenodo.3463003>). The idea behind the scattering database is that the users can use the scattering data of a desired zenith orientation or combine the data of different zenith orientations to mimic any desired distribution of zenith orientations. The scattering database is structured so that it can be used together with the scattering database of Eriksson et al. (2018). ~~The idea of our approach is to~~

To simulate the scattering of ice crystals properties, the scattering of ice crystal from various incidence directions ~~and then use these simulations for the orientation averages~~ is simulated and consequently used to calculate orientation averaged scattering. Similar to the work of Eriksson et al. (2018), Adams and Bettenhausen (2012), Hong et al. (2009) or Liu (2008) the scattering is simulated on the basis of the discrete dipole approximation (DDA, Draine and Flatau (1994)). Furthermore, the simulated scattering properties of ~~azimuthally randomly oriented~~ ice particles are used for radiative transfer simulations of cloudy scenes to investigate their influence on actual brightness temperature observations.

The text is structured as follows: in Sect. 2 we explain the particle orientation. Sect. 3 provides an overview of the basic setup and the simulated particles. Sect. 4 explains the scattering simulation. Sect. 5 shows some example results. Sect. 6 considers the influence of the simulated scattering properties in view of radiative transfer simulations. In Sect. 7 we summarize the results.

2 Particle orientation

Particle orientation refers to how the main axes of the particle are oriented with respect to the local horizon and the azimuthal reference. If the particle possesses spherical symmetry there is no particle orientation, because it does not matter from which side the particle with spherical symmetry is viewed or how it is rotated - it will always look the same. ~~As the~~ The particles considered in this paper ~~do not have a spherical symmetry they have an orientation~~ are not spherically symmetric and therefore can be oriented.

In general, the orientation of a particle in a ~~three-dimensional~~ three-dimensional space can be described by a set of three parameters. There is no unique set of these parameters. Depending on the definition of the rotation axes, there are different sets of these parameters. The three Euler angles are one such parameter set. The Euler angles define the orientation of the particle (coordinate) system relative to a fixed coordinate system, hereafter called laboratory system. The particle system is the coordinate system that is attached to the particle. This means, if a particle is rotated, the particle system is rotated the same way. The laboratory system stays under the rotation of the particle whereas the particle system changes its orientation. The laboratory system and particle system share the same origin. In this study, the Euler angles, which are shown in Fig. 1, are used according to the zyz' -notation. The particle is first rotated by angle α around the laboratory Z-axis, then the particle is rotated by angle β around the particle Y-axis (y') and last the particle is rotated by angle γ around the particle Z-axis. The value ranges

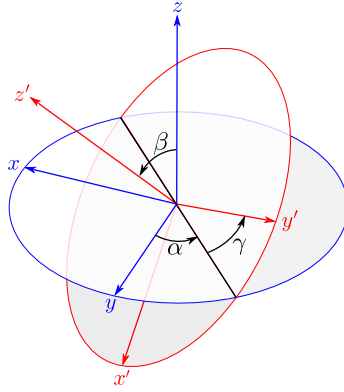


Figure 1. Euler angles

of the angles are

$$\alpha \in [0, 2\pi]$$

$$\beta \in [0, \pi]$$

$$\gamma \in [0, 2\pi]$$

(1)

These rotations are described by three orthogonal rotation matrices, see [Sect. Appendix B](#) for details. It is important to **know that** note that in general the order of the **rotation rotations** must not be changed, because the combination of rotations is generally not commutative.

Additionally In addition to the Euler angles, the orientation of the non-rotated particle is needed. As there is no absolute coordinate system, the orientation of the non-rotated particle is in general arbitrary. Therefore, we define that the non-rotated particle lies with its center of gravity at the origin of the laboratory system and all particle rotations will be relative to the origin of the laboratory system. The non-rotated particle is defined to have its principal moments of inertia axes aligned along the Cartesian coordinate axes, with the maximum inertia axis along the z-axis and the smallest along the x-axis (see Appendix A). This means for a plate-like particle that its longest dimensions lay parallel to the x-y-plane. This is the orientation that one intuitively expects for a falling plate-like particle in air. In reality the orientation of a particle determined by the balance of the gravitational force on one side and the drag force and other forces like e.g. electrical force on the other side (Khvorostyanov and Curry, 2014) . The drag force is determined by the interaction of particle and the surrounding air. Estimating the drag force is a challenging task, as one has to solve the Navier-Stokes equations for that. Klett (1995) modeled the orientation of falling ice columns. Under turbulent free conditions falling plates with diameters > 40 μm and columns with lengths > 30 μm are on average horizontally oriented. As most of the particles considered in our study are greater than 40 μm, we expect our definition for the non-rotated particle to be reasonable. Though we do not consider column-like particles in the study, the study of Klett (1995) suggests that even for them our definition is reasonable.

Within this study, we are not interested in the scattering of a single oriented particle but in the scattering of an ensemble of **oriented particles** particles, that are oriented differently but otherwise are identical. Generally, the scattering properties of

ensembles such an ensemble of oriented particles are described by averaging the single scattering properties over the three Euler angles, such that for example for the scattering matrix \mathbf{Z}_{eo} and the extinction matrix \mathbf{K}_{eo} of an ensemble of orientated particles hold

$$\mathbf{Z}_{eo}(\theta_{inc}, \phi_{inc}, \theta_s, \phi_s) = \int_0^{2\pi} \int_0^\pi \int_0^{2\pi} p_\alpha(\alpha) p_\beta(\beta) p_\gamma(\gamma) \mathbf{Z}(\theta_{inc}, \phi_{inc}, \theta_s, \phi_s, \alpha, \beta, \gamma) \sin\beta d\alpha d\beta d\gamma \quad (2)$$

$$\mathbf{K}_{eo}(\theta_{inc}, \phi_{inc}) = \int_0^{2\pi} \int_0^\pi \int_0^{2\pi} p_\alpha(\alpha) p_\beta(\beta) p_\gamma(\gamma) \mathbf{K}(\theta_{inc}, \phi_{inc}, \alpha, \beta, \gamma) \sin\beta d\alpha d\beta d\gamma \quad (3)$$

with θ_{inc} the incidence polar angle, ϕ_{inc} the incidence azimuth angle, θ_s the scattering polar angle and ϕ_s the scattering azimuth angle. $p_j(x)$ are probability density functions describing the distribution of particle orientation. Eq. 2 and 3 implicitly assume independent scattering, which is typically assumed in context of atmospheric radiative transfer. This means, that the scatterers are separated enough in distance, so that their scattered waves do not interact and that there are no systematic phase relations between the scattered waves (Mishchenko et al., 2000). In other words, Eq. 2 and 3 assume incoherent scattering.

We distinguish between two basic states of particle orientation

1. total random orientation (TRO) and
2. azimuthal random orientation (ARO).

Both orientation states are explained in the two following subsections.

2.1 Total random orientation

Totally randomly oriented particles are defined as the orientation average over the three Euler angles, in which the Euler angles are uniformly distributed. That is,

$$p_\alpha(\alpha) = p_\gamma(\gamma) = \frac{1}{2\pi} \quad (4)$$

$$p_\beta(\beta) = \frac{1}{\pi} \cdot \frac{\sin\beta}{2} \quad (5)$$

(Mishchenko and Yurkin, 2017). Due to this averaging, totally randomly oriented particles have effectively a spherical symmetry. This implies that the scattering matrix of totally randomly oriented particles depends only, like the scattering matrix of spheres, on the scattering angle Θ , i.e.

$$\mathbf{Z}_{tro}(\Theta) = \mathbf{Z}_{tro}(\theta_{inc}, \phi_{inc}, \theta_s, \phi_s), \quad (6)$$

and \mathbf{K}_{tro} will have no angular dependency. The scattering angle Θ

$$\Theta = \cos\theta_{inc}\cos\theta_s + \sin\theta_{inc}\sin\theta_s\cos(\phi_s - \phi_{inc}) \quad (7)$$

is the angle between incoming and outgoing direction. Eriksson et al. (2018), Ding et al. (2017), Liu (2008) and Hong et al. (2009) assume total random orientation in their databases.

2.2 Azimuthal random orientation

Azimuthally randomly oriented particles with a specific orientation to the horizon, also referred to as tilt or canting, are defined as the orientation average over α and γ , in which α and γ are uniformly distributed as for total random orientation. The scattering matrix \mathbf{Z}_{aro} and the extinction matrix \mathbf{K}_{aro} of azimuthally randomly oriented particles are thus calculated as

$$\mathbf{Z}_{\text{aro}}(\theta_{inc}, \theta_s, \Delta\phi, \beta) = \int_0^{2\pi} \int_0^{2\pi} p_\alpha(\alpha) p_\gamma(\gamma) \mathbf{Z}(\theta_{inc}, \phi_{inc}, \theta_s, \phi_s, \alpha, \beta, \gamma) d\alpha d\gamma \quad (8)$$

$$\mathbf{K}_{\text{aro}}(\theta_{inc}, \beta) = \int_0^{2\pi} \int_0^{2\pi} p_\alpha(\alpha) p_\gamma(\gamma) \mathbf{K}(\theta_{inc}, \phi_{inc}, \alpha, \beta, \gamma) d\alpha d\gamma \quad (9)$$

The averaging over α and γ results in a rotational symmetry of the scattering matrix to the laboratory Z-axis (cylindrical symmetry). The orientation average results in an effective particle shape as indicated in Fig. 2. To get a better picture of it, assume that the particle rotates very fast around the laboratory Z-axis and the particle Z-axis to symbolize the orientation averaging. By rotation it creates an effective solid of revolution. Changing the tilt angle β results in a different shape of this effective solid of revolution. Due to the cylindrical symmetry after orientation averaging, the averaged scattering matrix depends in azimuth only on the difference between incident and scattered azimuth direction. Whereas the scattering matrix of totally randomly oriented particles depends only on the scattering angle Θ , the scattering matrix of azimuthally randomly oriented particles depends on the incidence polar angle θ_{inc} , the scattering polar angle θ_s , the difference of the incidence and scattering azimuth angles $\Delta\phi = \phi_{inc} - \phi_s$ and the tilt angle β . Without any loss of generality, the azimuth incidence angle ϕ_{inc} is set to 0° for the azimuthally randomly oriented case from here on. It is important to note that the azimuthal symmetry does not mean that the scattering matrix \mathbf{Z}_{aro} is symmetric to incidence azimuth direction. This depends on the symmetry properties of the particles and the orientation of the rotation axes relative to the symmetry axes. To get a better idea of it, assume a flag rotates fast around its flagpole in counterclockwise direction as shown in Fig. 3. The flag has a white front side, a black-red frontside, a blue backside and its hoist is to the left. Independent from which side we look on the flagpole, the projections of the white frontside-red front side are always seen on the right side of the flagpole and the projections of the black-blue backside are always seen on the left side. If both sides of the flag have the same color then the projections on both sides will look the same. Although the rotation results in a rotational symmetry around the flagpole, the actual image we see depends on the symmetry properties of the flag.

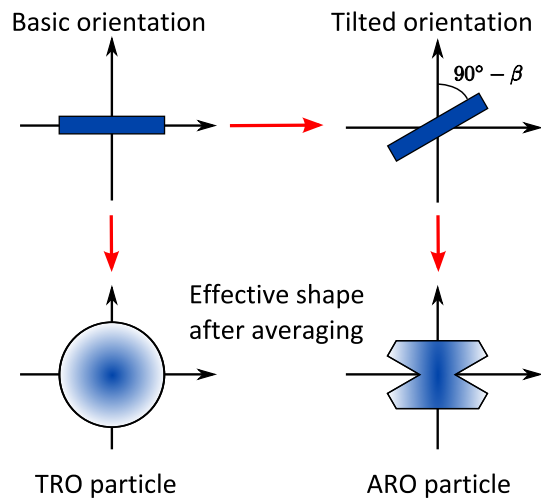


Figure 2. Schematic of the difference between totally random (TRO) and azimuthally random orientation (ARO).

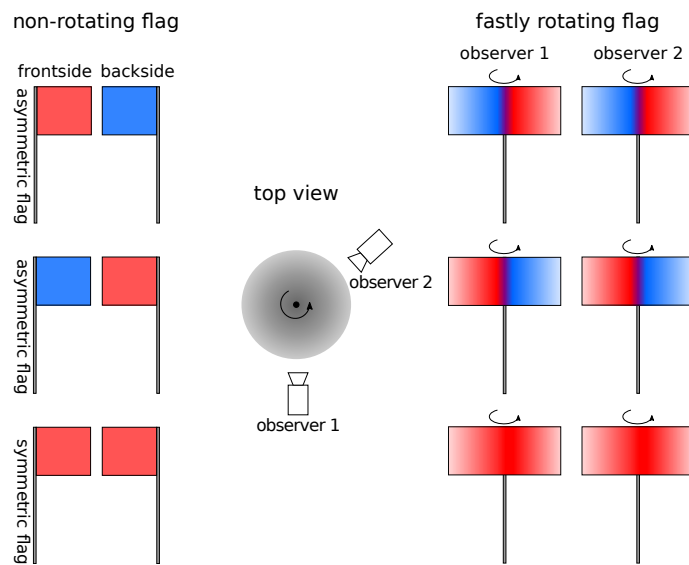


Figure 3. Schematic showing that rotation results in a rotational symmetry around the flagpole (axis). The actual image, that we see, depends on the symmetry properties of the flag (object).

3 Basic setup and shape data

The scattering calculations are computational demanding in view of computation time and the amount of data. Therefore, we have to compromise in terms of the accuracy of the resulting scattering data. Considering the measurement errors of existing and upcoming passive MW and SubMM sensors, which are in the order of $\mathcal{O}(1\text{K})$, and the brightness temperature depression due to scattering of frozen hydrometeors, which is typically $< 100\text{K}$, we aim for an accuracy of the scattering database in the order of a few percent.

For the scattering calculations ~~Amsterdam DDA (ADDA)~~ ADDA version 1.2 was used. ADDA is a DDA implementation of Yurkin and Hoekstra (2011). The basic idea of DDA is to represent the particle by a discrete set of electric dipoles. ~~For To~~ calculate the scattering, ADDA iteratively solves the linear system

$$\alpha_i P_i - \sum_{i \neq j} H_{ij} P_j = E_{inc,i} \quad (10)$$

with i, j the dipole indices, α_i the dipole polarizability, P_i the unknown dipole polarization, H_{ij} the interaction term and $E_{inc,i}$ the incident electric field. The resulting scattering quantities of ADDA are derived from the solution of the dipole polarization P_i , for details see Yurkin and Hoekstra (2011). The iteration is stopped when the relative norm of the residuals ϵ is less than a user specified value. The relative norm of the residuals ϵ is essentially the relative difference between the left-hand side and the right-hand side of Eq. 10. To reduce the computation time in view of our desired accuracy for the scattering database, we set the relative norm of the residuals to

$$\epsilon = 10^{-2}. \quad (11)$$

For further details of the DDA method, see Yurkin and Hoekstra (2011) and the references therein.

ADDA can simulate the scattering of totally randomly oriented particles and the scattering of particles with a fixed but arbitrary orientation. The internal averaging method of ADDA ~~cannot be used for is not suitable for our approach to simulate~~ azimuthally oriented particles. Instead, we developed an averaging approach that involves integration over a set of DDA calculations at different angles, ~~and transformations of reference frames~~, which is explained in Sect. 4.

For DDA simulations it is important that the size of the dipoles is small compared to the wavelength and to any structural length within the scatterer (Yurkin and Hoekstra, 2011). For all particles considered in our study holds

$$|m|kd < \frac{1}{2} \quad (12)$$

with m the refractive index of ice, k the angular wavenumber and d the dipole size. With the microwave refractive index of ice this results in ≈ 22 dipoles per wavelength. Furthermore, all simulated particles consist of at least 1,000 dipoles so that small particles are reasonably resolved.

Following Eriksson et al. (2018), we organize the different particle shapes as habits. A habit is defined as a set of particles of different sizes with a common basic morphology, roughly following a mass-size relationship. In this work we consider two different types of frozen hydrometeor habits:

Table 1. Overview of the selected habits. a - and b - are the parameters of the mass-size relationship (Eq. 13), D_{veq} is the volume equivalent diameter and D_{max} is the maximum diameter. ID is the identification number from the database of Eriksson et al. (2018).

habit name	ID	type	a [kg]	b	No. of sizes	D_{veq} [μm]	D_{max} [μm]
plate type 1	9	single crystal	0.76	2.48	51	10 – 2,596	13 – 10,000
large plate aggregate	20	aggregate	0.21	2.26	18	197– 4,563	349– 22,860

- plate type 1, which is a solid hexagonal plate-like single crystal, and
- large plate aggregate, which consists of several solid hexagonal plates aggregated to one particle.

200 [Fig. 4 shows some different sized particles of both habits as example.](#) The shape data including the actual dipole grids for ADDA were taken from the database of Eriksson et al. (2018). ~~Following Eriksson et al. (2018), a habit is defined as a set of particles of different sizes, roughly following a mass-size relationship.~~ The mass-size relationship is defined as

$$m = a \left(\frac{D}{D_0} \right)^b \quad (13)$$

with m the particle mass, D the maximum diameter, D_0 the unit diameter $D_0 = 1 \text{ m}$ and the parameters a , b . [The maximum diameter is defined as the diameter of the minimum circumscribed sphere of a particle.](#) Table 1 shows for each habit the size range and the values of the parameters a , b . ~~Fig. 4 shows some different sized particles of both habits as example.~~ For the plate type 1 habit, 51 differently sized particles were simulated. The size range is between $10 \mu\text{m}$ and $2,596 \mu\text{m}$ volume equivalent diameter, which corresponds to maximum diameters between $13 \mu\text{m}$ and $10,000 \mu\text{m}$. The [volume equivalent diameter is defined as the diameter of a solid ice sphere with the same mass as the particle.](#) The plate type 1 habit in our study has slightly different sizes than the plate type 1 in Eriksson et al. (2018), [because an older version of shape data was used than in Eriksson et al. \(2018\) and given the high computational costs of the scattering calculation a recalculation was not feasible.](#) For the large plate aggregate habit, 18 differently sized particles were simulated. The size range is between $197 \mu\text{m}$ and $4,563 \mu\text{m}$ volume equivalent diameter, which corresponds to maximum diameters between $349 \mu\text{m}$ and $22,860 \mu\text{m}$. For details on the particle shape data the reader is referred to Eriksson et al. (2018).

215 In this work we follow the approach of Eriksson et al. (2018) for the temperature and frequency selection. The selected frequency range of the scattering calculation consists of 35 frequencies between 1 GHz and 864 GHz. Most selected frequencies are organized to include channel sets of existing and planned submillimeter and microwave radiometers. Table 2 shows the selected frequencies. ~~The~~ [Due to a rounding mistake when the simulation was set up, the](#) frequencies of the plate type 1 habit slightly deviate from the frequencies of the large plate aggregate habit by at maximum 0.5 GHz. The selected temperatures are 190 K, 230 K, and 270 K. Following Eriksson et al. (2018), the refractive index of ice is calculated by the model of Mätzler
220 (2006).

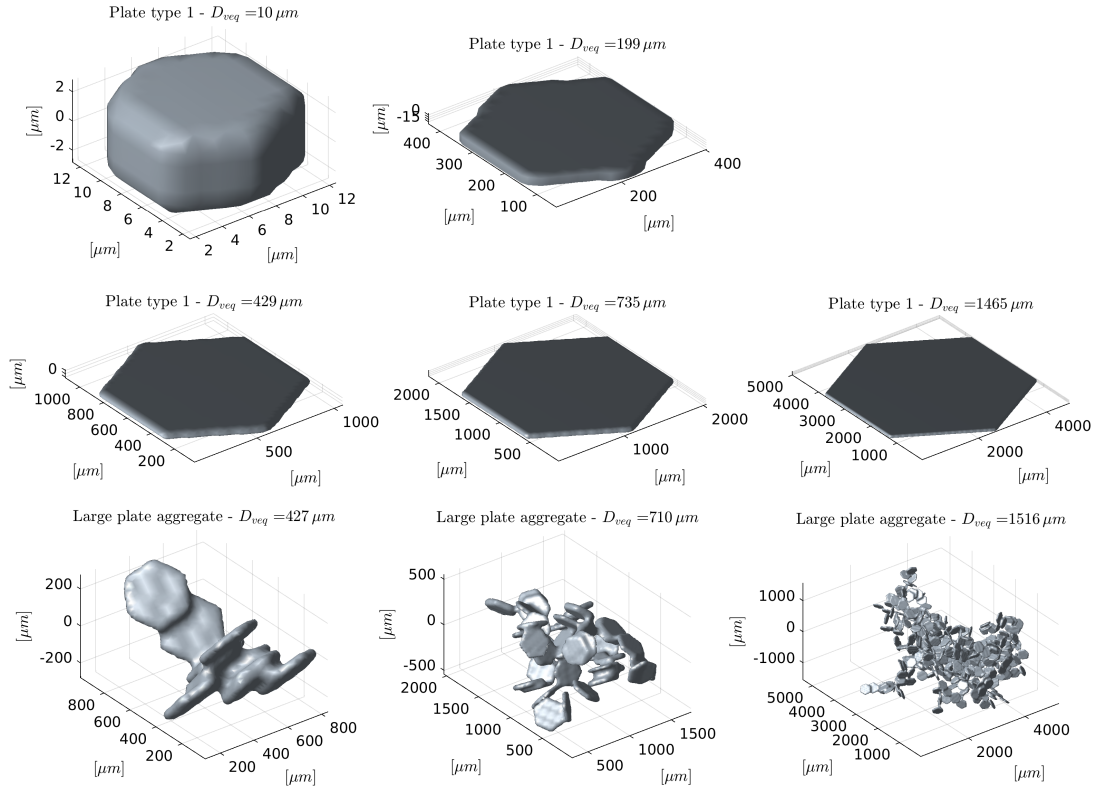


Figure 4. Example scatterer shapes.

Table 2. The frequencies for the scattering calculations. Except for 35.6GHz, the channels ≥ 18.6 GHz are organized in channel sets, see text.

Channel set	1	2	3	4	5	6	7	8	9	10	11	12
Freq.	18.6	31.3	50.1	88.8	115.3	164.1	175.3	228	314.2	439.3	657.3	862.4
[GHz]	24	31.5	57.6	94.1	122.2	166.9	191.3	247.2	336.1	456.7	670.7	886.4
Other frequencies [GHz]:												
1, 1.4, 3, 5, 7, 9, 10, 10.65, 13.4, 15, 35.6												

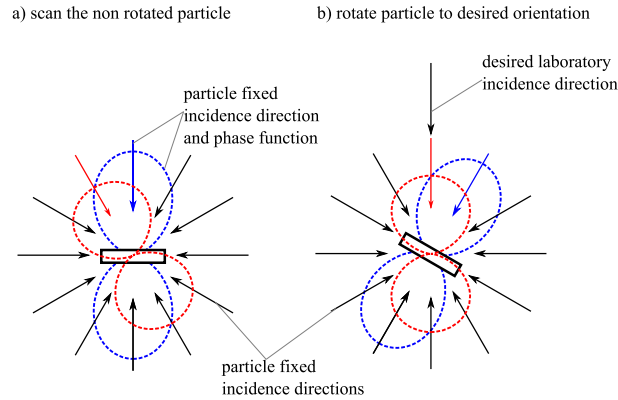


Figure 5. Schematic drawing of the calculation of the single scattering properties. (left) the non rotated particle with the incidence and scattering directions fixed to the particle. (right) the rotated particle and the rotated incidence and scattering directions.

4 Scattering calculations

In general, the scattering matrix Z of a non-spherical particle depends on the incidence direction $(\theta_{inc}, \phi_{inc})$, the scattering direction (θ_s, ϕ_s) and the particle orientation described by the three Euler angles α, β and γ . The same holds for the extinction matrix K except that it is independent of the scattering directions. The rotation of a particle is equivalent to the inverse rotation of the incidence direction. This means, it is equivalent if the scattering of a particle is calculated for any incidence angle at a fixed orientation or if the scattering of a particle is calculated for any orientation but at a fixed incidence angle. This equivalence is the key point in our approach. Therefore the scattering is calculated for any incidence direction and scattering direction and the particle orientation is kept fixed. The orientation averaging is calculated by rotating the incidence and scattering direction according to the particle orientation. With ADDA it is only possible to calculate the scattering properties for a finite set of incidence and scattering directions. ~~SoHence~~, the scattering matrix and the extinction matrix are calculated for a set of different incidence directions and scattering directions (only scattering matrix). The result is the scattering matrix and the extinction matrix for finite set of incidence and scattering directions, which are fixed to the particle, see Fig. 5 a. For a specific orientation of the particle, the set of incidence and scattering directions are rotated ~~aeordingly-according~~ to the orientation of the particle, see Fig. 5 ~~b. This approach is analogue to the analytic T-matrix method, only in a much more numerical way. b.~~

The actual results of an ADDA calculation are the scattering amplitude matrix and the Mueller matrix for a desired incidence direction and a grid of scattering directions, whereas we are interested in extinction matrix and scattering matrix. The relationship between the scattering amplitude matrix and the extinction matrix and between the Mueller matrix and the scattering matrix are explained in the following paragraphs. Difficulties arise from the fact that the matrices are defined in different coordinate systems. The scattering matrix and the extinction matrix for the scattering database are defined in the laboratory system. The extinction matrix that results from the scattering amplitude matrix and the Mueller matrix are defined in the coordinate system that is defined by the incidence direction and the particle system, from here on called wave reference system. Due to the relation to the particle system the wave reference system rotates if the particle (particle system) rotates.

Therefore the main part of our averaging approach consists essentially of transformations from one coordinate system to another coordinate system.

245 The extinction matrix \mathbf{K} depends on the scattering amplitude matrix for the forward direction ($\theta_{inc} = \theta_s$, $\phi_{inc} = \phi_s$, Mishchenko et al. 2002)

$$\mathbf{K}\mathbf{K} = \frac{2\pi}{k} \begin{pmatrix} \text{Im}(S_{11} + S_{22}) & \text{Im}(S_{11} - S_{22}) & -\text{Im}(S_{12} + S_{21}) & \text{Re}(S_{21} - S_{12}) \\ \text{Im}(S_{11} - S_{22}) & \text{Im}(S_{11} + S_{22}) & \text{Im}(S_{21} - S_{12}) & -\text{Re}(S_{12} + S_{21}) \\ -\text{Im}(S_{12} + S_{21}) & -\text{Im}(S_{21} - S_{12}) & \text{Im}(S_{11} + S_{22}) & \text{Re}(S_{22} - S_{11}) \\ \text{Re}(S_{21} - S_{12}) & \text{Re}(S_{12} + S_{21}) & -\text{Re}(S_{22} - S_{11}) & \text{Im}(S_{11} + S_{22}) \end{pmatrix} \quad (14)$$

with the scattering amplitude matrix

$$\mathbf{S}\mathbf{S} = \begin{pmatrix} S_{11} & S_{12} \\ S_{21} & S_{22} \end{pmatrix} = \frac{1}{-ik} \begin{pmatrix} s_2 & s_3 \\ s_4 & s_1 \end{pmatrix}, \quad (15)$$

250 k the angular wave-number wavenumber and s_j the scattering amplitude matrix element of ADDA. The scattering amplitude is a complex matrix and operates on the complex electric field, whereas the extinction, the scattering, and the Mueller matrix operate on the Stokes vector, which is a real vector. Between the scattering matrix \mathbf{Z} and the Mueller matrix $\mathbf{M}\mathbf{M}$, which are both real 4×4 matrices, following linear relationship holds

$$\mathbf{Z} = \frac{1}{k^2} \mathbf{L}\mathbf{L}_s \mathbf{M}\mathbf{L}\mathbf{M}\mathbf{L}_i \quad (16)$$

255 with $\mathbf{L}_i, \mathbf{L}_s$ the Stokes $\mathbf{L}_j, \mathbf{L}_s$ the Stokes rotation matrices (Mishchenko et al., 2002). The Stokes rotation matrices transform the Mueller matrix from the wave reference system to the laboratory system. The Stokes rotation matrices $\mathbf{L}_{i,s}, \mathbf{L}_{i,s}$ are defined in Sect. D. Due to the linear relationship, it does not matter if first the Mueller matrix is transformed to a scattering matrix and then the scattering matrix is averaged or vice versa. Instead of transforming every calculated Mueller matrix into the scattering matrix, the averaging will be done for the Mueller matrix and at the end the averaged Mueller matrix is transformed to the scattering matrix, which is described in Sect. Appendix D.

260 Each Mueller matrix element $M_{ij}(\theta_{inc}, \phi_{inc}, \theta'_s, \phi'_s)$, which has a scattering direction grid spacing of 1° , is expanded as a spherical harmonics series over the scattering directions θ'_s, ϕ'_s (see Appendix ??E) to efficiently store the results of the ADDA calculation. The prime denotes that the angles are related to the incidence direction wave reference system and not to the laboratory system as the unprimed angles. To reduce the amount of data, the spherical harmonic series is truncated to the number of coefficients, for which the mean square error between the series expansion and the original representation is less than 0.5% of the standard deviation of the M_{11} element over the scattered direction. The relation to the M_{11} element results on average that after the truncation features of the other Mueller matrix elements are still resolved, if their magnitude is greater than the truncation error of M_{11} . This allows to resolve the relevant features given the desired accuracy of the scattering database and reduces the amount of data by up to two orders of magnitude.

270 For each incidence direction, ADDA automatically calculates the Mueller matrix for a desired regular grid of polar angles and azimuth angles. A regular grid of polar and azimuth angles has the property that the grid spacing at the pole is much finer

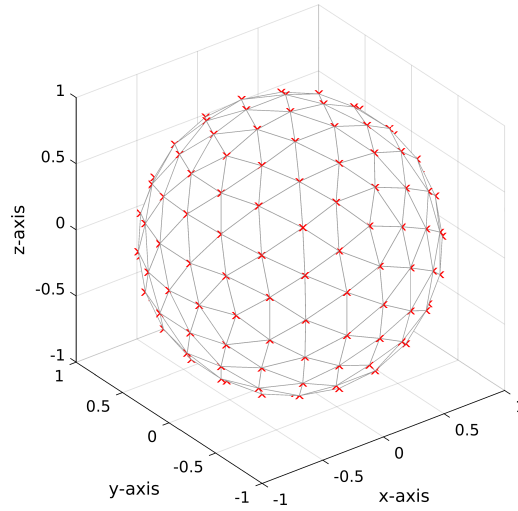


Figure 6. Example of an icosphere grid with 162 vertices. Each gridpoint represent an incoming angle for which a DDA calculation is ~~performed~~performed. This type of configuration ensures that the grid density is isotropic, making the overall calculations more efficient (a standard polar grid would be inefficient since it yields an excessive amount of angles around the ‘North and South poles’’).

than at the equator. ~~Actually, this is advantageous for scattering, because due to the definition of the Mueller matrix the forward peak and the backward peak are located at the poles.~~

For the set of incidence angles, a regular grid of polar angles and azimuth angles are disadvantageous, because for the
 275 incidence angle an isotropic sampling is needed but the distribution of the directions of a regular grid of polar angles and
 azimuth angles is not isotropic. Therefore, an icosahedral grid is used, which is shown in Fig. 6. An icosahedral grid is almost
 isotropic. The distances between two neighboring vertices (grid points) is everywhere the same and an icosahedral grid ~~consist~~
~~consists~~ of equilateral triangles, which have all the same size. This makes the icosahedral grid convenient for grid refinement
 and adjusting the grid size for the needed accuracy. An icosahedral grid can be set up by recursively bisecting the edges of an
 280 icosahedron and projecting the new vertices on a sphere. Such an icosahedral grid consists of

$$N_v = 10 \cdot (2l)^2 + 2 \tag{17}$$

vertices and

$$N_t = 20 \cdot (2l)^2 \tag{18}$$

triangles with l the refinement level. The coordinates of the vertices of the icosahedral grid on the unit sphere are the set
 285 incidence directions. For more details on icosahedral grids, see for example Satoh (2014). ~~For the scattering calculations~~
~~between 162 and 2562 incidence angles were used depending on the partiele size and shape.~~

The ~~actual orientation averaging is done by approximating orientation averaged Mueller matrix M_{aro} is~~

$$\underline{MM}_{aro}(\theta_{inc}, \theta'_s, \phi'_s, \beta) = \int_0^{2\pi} \int_0^{2\pi} p_\alpha(\alpha) p_\gamma(\gamma) R_{\alpha\beta\gamma}^* (\underline{MM}) d\alpha d\gamma \quad (19)$$

and ~~orientation averaged extinction matrix K_{aro} is~~

$$290 \quad \underline{KK}_{aro}(\theta_{inc}, \beta) = \int_0^{2\pi} \int_0^{2\pi} p_\alpha(\alpha) p_\gamma(\gamma) R_{\alpha\beta\gamma}^* (\underline{KK}) d\alpha d\gamma \quad (20)$$

~~with a twofold with Gauss-Legendre quadrature.~~ The rotation operator $R_{\alpha\beta\gamma}^*$ rotates the Mueller and the extinction matrix according to the desired orientation, which is explained in [SectAppendix](#). B. The needed interpolation is done by using a barycentric interpolation for triangles, which is explained in [appendix-Appendix](#) C. Afterwards the averaged Mueller matrix ~~$\underline{M}_{aro}(\theta_{inc}, \theta'_s, \phi'_s, \beta)$~~ ~~$\underline{M}_{aro}(\theta_{inc}, \theta'_s, \phi'_s, \beta)$~~ is transformed into the scattering matrix \underline{Z}_{aro} using Eq. 16, which is explained in [SectAppendix](#). D. As mentioned in Sect. 2.2, the resulting scattering matrix \underline{Z}_{aro} is in general not symmetric ~~to the incidence angle~~, as this depends on the actual particle. The scattering matrix \underline{Z}_{aro} is symmetric if it is averaged with its own mirrored version, in which it is reflected relative to the plane of incidence direction and laboratory Z-axis. This is equivalent to having simulated the scattering of the desired particle and its mirrored version, in which it is reflected by a plane that includes the laboratory Z-axis, [see Mishchenko et al. \(2002\) or van de Hulst \(1981\) for further details on the symmetry of the scattering](#)
300 [matrix.](#)

[The actual scattering calculations are done iteratively. For each particle, the scattering calculation begins with 12 incidence angles \(refinement level \$l = 0\$ \). With each additional refinement level \$l\$ the number of incidence angles increases according to Eq. 17 roughly by a factor of four. With each iteration step the edges of the triangles of the icosahedral grid are bisected creating new vertices \(incidence angles\). This means that the incidence angles of the previous iteration are part of the grid for](#)
305 [the current iteration. Due to that only about \$\frac{3}{4}\$ of the number of incidence angles have to be calculated for each iteration step. The iteration stops when](#)

$$\frac{\delta_{l,l-1}}{\delta_{l-1,l-2}} \leq 10^{-2}. \quad (21)$$

[The change \$\delta_{l,l-1}\$ between the current iteration step \$l\$ and the previous iteration step is defined as the summed root mean square differences between the upper left block of the orientation averaged extinction matrix of iteration step \$l\$ and \$l - 1\$ for](#)
310 [five different tilt angles \$\beta\$ and ten incidence angles \$\theta_{inc}\$. Depending on the particle size and shape, between 162 and 2562 incidence angles were used.](#)

[To test our approach, the scattering of azimuthally randomly oriented prolate ellipsoids with an aspect ratio of 0.5 for several size parameters were simulated and compared with results from T-matrix calculations. The overall differences in view of the extinction matrix and the scattering matrix were in the order of a few percent.](#)

315 The methodology to calculate the scattering matrix and the extinction matrix can be summarized as:

1. DDA calculations: A set of DDA runs are performed over an icosahedral angle grid of incidence directions, demonstrated in Fig. 6. This type of grid ensures that the angle density is isotropic and increases the efficiency.
2. Represent the Mueller matrix elements of each ADDA run in a spherical harmonics series and truncate them to reduce the amount of data.
- 320 3. Averaging: Azimuthally averaged Mueller matrices $\underline{\mathbf{M}}_{aro}(\theta_{inc}, \theta'_s, \phi'_s, \beta)$ and extinction matrices $\underline{\mathbf{K}}_{aro}(\theta_{inc}, \beta)$ for a set of tilt angles β and polar incidence angles θ_{inc} are calculated by integrating the Mueller and extinction matrices over the Euler angles α and γ .
4. Transformation: The averaged Mueller matrices are transformed to averaged scattering matrices $\underline{\mathbf{Z}}_{aro}$.

4.1 Particle rotation

325 ~~The key point in our averaging approach is the rotation of the particle for the averaging process. When rotating the particle the incidence and scattering direction change. The changed direction $\hat{\mathbf{e}}_{i,rot}$ for a desired orientation is given by~~

~~$$\hat{\mathbf{e}}_{i,rot} = \mathbf{R}_{\alpha\beta\gamma} \hat{\mathbf{e}}_i$$~~

~~with $\hat{\mathbf{e}}_i$ the non-rotated incidence or scattering direction and $\mathbf{R}_{\alpha\beta\gamma}$ the rotation matrix. The rotation matrix $\mathbf{R}_{\alpha\beta\gamma}$ is~~

~~$$\mathbf{R}_{\alpha\beta\gamma} = \mathbf{R}(\alpha) \mathbf{R}(\beta) \mathbf{R}(\gamma) = \begin{pmatrix} R_{11} & R_{12} & R_{13} \\ R_{21} & R_{22} & R_{23} \\ R_{31} & R_{32} & R_{33} \end{pmatrix}$$~~

330 ~~with the Euler angles α , β , and γ . See Appendix ?? for the rotation matrix elements R_{ij} . When the incidence and scattering directions change, the polarization directions change, too. The polarization directions of each simulated Mueller matrix and extinction matrix are fixed to their original incidence direction. This means the original polarization directions of the Mueller matrix and the extinction matrices change under rotation as indicated in Fig. B1. The rotation about the laboratory Z-axis by the Euler angle α does not change the polarization, because the vertical polarization direction stays always in the plane spanned~~

335 ~~by incidence direction unit vector $\hat{\mathbf{e}}_{ki}$ and the laboratory z-axis and the horizontal polarization direction stays parallel to the x-y-plane. But the combined rotations by the Euler angles β and γ do change. After the combined rotation the original vertical polarization unit vector $\hat{\mathbf{e}}_v$ is rotated out of the plane spanned by incidence direction unit vector $\hat{\mathbf{e}}_{ki}$ and the laboratory z-axis by angle φ and original horizontal polarization unit vector $\hat{\mathbf{e}}_h$ is rotated out of the x-y-plane by angle φ . After the rotation using $\mathbf{R}_{\alpha\beta\gamma}$ the polarization of the Mueller matrix $\underline{\mathbf{M}}$ and the extinction matrix $\underline{\mathbf{K}}$ need to be transformed to the laboratory~~

340 ~~polarization using the Stokes rotation matrix $\underline{\mathbf{L}}$ (Mishchenko et al., 2002)~~

$$\mathbf{L}(\varphi) = \begin{pmatrix} 1 & 0 & 0 & 0 \\ 0 & \cos 2\varphi & -\sin 2\varphi & 0 \\ 0 & \sin 2\varphi & \cos 2\varphi & 0 \\ 0 & 0 & 0 & 1 \end{pmatrix}.$$

The Mueller matrix \mathbf{M}_{rot} and the extinction matrix \mathbf{K}_{rot} of the rotated particle are given by

$$\mathbf{M}_{rot} = R_{\alpha\beta\gamma}^*(\mathbf{M}) = \mathbf{L}(\varphi) \mathbf{M}(\mathbf{R}_{\alpha\beta\gamma}(\theta_{inc}, \phi_{inc}), \mathbf{R}_{\alpha\beta\gamma}(\theta'_s, \phi'_s)) \mathbf{L}(-\varphi)$$

and

$$345 \quad \mathbf{K}_{rot} = R_{\alpha\beta\gamma}^*(\mathbf{K}) = \mathbf{L}(\varphi) \mathbf{K}(\mathbf{R}_{\alpha\beta\gamma}(\theta_{inc}, \phi_{inc})) \mathbf{L}(-\varphi).$$

The rotation angle φ is

$$\varphi = \text{atan2}(\hat{\mathbf{e}}_v \cdot \hat{\mathbf{e}}_{h,lab}, \hat{\mathbf{e}}_v \cdot \hat{\mathbf{e}}_{v,lab})$$

with the rotated vertical polarization direction $\hat{\mathbf{e}}_v$, the horizontal polarization direction in the laboratory system

$$\hat{\mathbf{e}}_{h,lab} = \hat{\mathbf{e}}_{v,lab} \times \hat{\mathbf{e}}_{ki},$$

350 the vertical polarization direction in the laboratory system

$$\hat{\mathbf{e}}_{v,lab} = (\hat{\mathbf{e}}_z \times \hat{\mathbf{e}}_{ki}) \times \hat{\mathbf{e}}_{ki},$$

and z-direction $\hat{\mathbf{e}}_z$.

Change of the polarization directions under rotation. (top left) the incidence direction unit vector $\hat{\mathbf{e}}_{ki}$ together with the vertical polarization unit vector $\hat{\mathbf{e}}_v$ and the horizontal polarization unit vector $\hat{\mathbf{e}}_h$, which are fixed to the particle, before the rotation is performed. (top right) the unit vectors after the rotation by angle β and (bottom right) after the rotation by angle γ . As indicated (bottom left) the polarization vectors after the rotation by angles β and γ are twisted by angle φ compared to the laboratory unit vectors.

4.1 Transformation of the averaged Mueller matrix to the averaged scattering matrix

Between the scattering matrix averaged \mathbf{Z} and the averaged Mueller matrix \mathbf{M} following relationship holds

$$360 \quad \mathbf{Z}(\theta_{inc}, \theta_s, \phi_s, \beta) = \frac{1}{k^2} \mathbf{L}(-\varphi_s) \mathbf{M}(\theta_{inc}, R(\theta'_s, \phi'_s), \beta) \mathbf{L}(\varphi_i)$$

with k the angular wave number, \mathbf{L} the stokes rotation matrix (Eq. B12), φ_i, φ_s the polarization rotation angles, and $R(\theta'_s, \phi'_s)$ the rotation operator that transforms the incidence direction related coordinate system to the laboratory system.

As defined in Sect. 2.2, the incidence azimuth direction is zero. In that case the incidence direction vector is always within the X-Z-plane. The rotation operator $R(\theta'_s, \phi'_s)$ then is

$$365 \quad \begin{pmatrix} \theta_s \\ \phi_s \end{pmatrix} = R \begin{pmatrix} \theta'_s \\ \phi'_s \end{pmatrix} = \begin{pmatrix} \arccos(-\sin \theta_{inc} \sin \theta'_s \cos \phi'_s + \cos \theta_{inc} \cos \theta'_s) \\ \text{atan2}(\sin \theta'_s \sin \phi'_s, \cos \theta_{inc} \sin \theta'_s \cos \phi'_s + \sin \theta_{inc} \cos \theta'_s) \end{pmatrix}.$$

The stokes rotation matrices $\mathbf{L}(-\varphi_s), \mathbf{L}(\varphi_i)$ transform the polarization basis from relative to the scattering direction to relative to incidence direction. Fig. D1 shows the geometry for polarization basis transformation. Scattering geometry in the laboratory system The stokes rotation matrix $\mathbf{L}(-\varphi_s)$ describes the rotation by angle φ_s , which is the angle between the plane, that is spanned by the unit vector of the scattering direction $\hat{\mathbf{e}}_{k_s}$ and the laboratory Z-axis, and the scattering plane, which is

370 the plane that is spanned by the unit vector of the incidence direction $\hat{\mathbf{e}}_{k_i}$ and the unit vector of the scattering direction $\hat{\mathbf{e}}_{k_s}$. The stokes rotation matrix $\mathbf{L}(\varphi_i)$ describes the rotation by angle φ_i , which is the angle between the plane that is spanned by the unit vector of the incidence direction and the laboratory Z-axis, and the scattering plane. The unit vector $\hat{\mathbf{e}}_{k_j}$ describing the incidence or scattering direction is

$$\hat{\mathbf{e}}_{k_j} = \begin{pmatrix} \sin \theta_j \cos \phi_j \\ \sin \theta_j \sin \phi_j \\ \cos \theta_j \end{pmatrix}$$

375 and the unit vector of the vertical polarization $\hat{\mathbf{e}}_{vj}$ for the incidence direction or the scattering direction is

$$\hat{\mathbf{e}}_{vj} = \begin{pmatrix} \cos \theta_j \cos \phi_j \\ \cos \theta_j \sin \phi_j \\ -\sin \theta_j \end{pmatrix}$$

with $j = i, s$ for the incidence direction and the scattering direction, respectively. The rotation angle is

$$\varphi_j = \begin{cases} -\arccos(\hat{\mathbf{e}}_{vj} \cdot \hat{\mathbf{p}}_j) & , \hat{\mathbf{e}}_{vj} \cdot \hat{\mathbf{n}}_j \geq 0 \\ \arccos(\hat{\mathbf{e}}_{vj} \cdot \hat{\mathbf{p}}_j) & , \hat{\mathbf{e}}_{vj} \cdot \hat{\mathbf{n}}_j < 0 \end{cases}.$$

with the unit vector

$$380 \quad \hat{\mathbf{p}}_j = \hat{\mathbf{n}} \times \hat{\mathbf{e}}_{kj}$$

that is parallel to scattering plane and orthogonal to $\hat{\mathbf{e}}_{kj}$. The normal vector

$$\hat{\mathbf{n}} = \frac{\hat{\mathbf{e}}_{ks} \times \hat{\mathbf{e}}_{ki}}{\sin \Theta}$$

is orthogonal to the scattering plane. The scattering angle Θ , which is the angle between the incidence direction and the scattering direction is

$$\sin \Theta = |\hat{\mathbf{e}}_{ks} \times \hat{\mathbf{e}}_{ki}|$$

In the actual implementation each matrix element $M_{ij,aro}(\theta_{inc}, \theta'_s, \phi'_s)$ of the averaged Mueller matrix is represented as a spherical harmonics series over the scattering directions θ'_s, ϕ'_s . For the calculation of the averaged scattering matrix $\underline{\mathbf{Z}}_{aro}$, the Mueller matrix elements $M_{ij,aro}(\theta_{inc}, \theta'_s, \phi'_s)$ in angular grid representation are used. The resulting scattering matrix elements $\underline{\mathbf{Z}}_{ij,aro}$ in angular grid representation are expanded afterwards as spherical harmonics series over the scattering directions θ_s, ϕ_s .

5 Results of the scattering simulations

In this section we give an overview of the scattering simulations and show some example results. 51 sizes of plate type 1 (hexagonal plate) and 18 sizes of large plate aggregates for 35 frequencies and 3 temperatures were simulated. The simulations were conducted on DKRZ's (Deutsches Klimarechenzentrum) supercomputer Mistral. This took about $1.6 \cdot 10^6$ core hours on Intel Xeon E5-2695V4 processors with a clock rate of ~~2.1GHz~~ 2.1GHz. The amount of data of the scattering calculations is huge. Whereas the scattering matrix $\mathbf{Z}_{tro}(\Theta)$ for total random orientation depends on one angle, the scattering matrix $\mathbf{Z}_{aro}(\theta_{inc}, \theta_s, \phi_s)$ for azimuthal random orientation depends on three angles. Furthermore, the tilt angle β adds an additional dimension. This leads to an up to three orders of magnitude larger amount of data. To reduce the ~~computation time and the amount of data, ADDA was used with an accuracy of $\epsilon = 1\%$~~ computational time, the residual relative norm, which is the stopping criterion of ADDA's iterative solver, was set to 10^{-2} following Eriksson et al. (2018). The Mueller and the scattering matrices for a given incidence angle were represented in a truncated spherical harmonics series. with an accuracy of 0.5% to reduce the amount of data. Even then, the total size of the data from the DDA simulations is about 1.5TB. Due to the orientation averaging the amount of data reduces to about 0.18TB.

The orientation averaging is done for a finite set of incidence and tilt angles. The incidence angles θ_{inc} span a range from 0° to 180° with a 5° spacing and the tilt angles β span a range from 0° to 90° for plate type 1 and from 0° to 180° for large plate aggregates with a 10° spacing. The tilt angle range for plate type 1 is confined to 90° , because of its mirror symmetry to the x-y plane. In this case it holds for the scattering matrix \mathbf{Z}_{aro} and the extinction matrix \mathbf{K}_{aro} that

$$\begin{aligned} \mathbf{Z}_{aro}(\theta_{inc}, \theta_s, \phi_s, \beta) &= \mathbf{Z}_{aro}(\theta_{inc}, \theta_s, \phi_s, \pi - \beta) \\ \mathbf{K}_{aro}(\theta_{inc}, \beta) &= \mathbf{K}_{aro}(\theta_{inc}, \pi - \beta). \end{aligned} \tag{22}$$

The scattering database with the orientation averaged data is publicly available from Zenodo (<https://doi.org/10.5281/zenodo.3463003>). The data from the DDA simulations is available upon request from us. The scattering database is organized so that the Python 3 interface of the database of Eriksson et al. (2018) can be used to extract and interact with the data. The scattering database additionally includes the absorption vector \mathbf{a} for each incidence and tilt angle ~~the absorption vector \mathbf{a}~~ . The

i -th component of the absorption vector is

$$a_i(\theta_{inc}, \beta) = K_{aro,i1}(\theta_{inc}, \beta) - \int_0^{2\pi} \int_0^{\pi} Z_{aro,i1}(\theta_{inc}, \theta_s, \phi_s, \beta) d\phi_s d\theta_s \quad (23)$$

415 with $K_{aro,i1}$ and $Z_{aro,i1}$ the i -th component of the first column of the extinction matrix \mathbf{K}_{aro} and scattering matrix \mathbf{Z}_{aro} (Mishchenko et al., 2000).

In the following analysis we will not address the absorption vector, because it is derived directly from the extinction and scattering matrix and is just added to the database for convenience.

5.1 Extinction matrix and asymmetry parameter

420 The orientation averaging (Eq. 20) reduces Eq. 14 to

$$\mathbf{K}\mathbf{K}_{aro} = \frac{2\pi}{k} \begin{pmatrix} \text{Im}(S_{11} + S_{22}) & \text{Im}(S_{11} - S_{22}) & 0 & 0 \\ \text{Im}(S_{11} - S_{22}) & \text{Im}(S_{11} + S_{22}) & 0 & 0 \\ 0 & 0 & \text{Im}(S_{11} + S_{22}) & \text{Re}(S_{22} - S_{11}) \\ 0 & 0 & -\text{Re}(S_{22} - S_{11}) & \text{Im}(S_{11} + S_{22}) \end{pmatrix} \quad (24)$$

with S_{ii} the scattering amplitude matrix elements (Eq. 15) and k the angular [wave number](#). Whereas the extinction matrix has seven independent entries in general, the extinction matrix for azimuthal random orientation has only three independent entries that depend on the incidence angle θ_{inc} and the tilt angle β . For total random orientation the extinction matrix has only one independent entry that is constant.

Fig. 7 and Fig. 8 show the [three](#) independent entries of the extinction matrix (K_{11} , K_{21} , and K_{43}) of plate type 1 and large plate aggregate at 671 GHz for several tilt angles β and size parameters x

$$x = ka_{eq} = \frac{2\pi a_{eq}}{\lambda} = \frac{\pi D_{eq}}{\lambda} \quad (25)$$

with a_{eq} the volume equivalent frozen radius, D_{eq} the volume equivalent frozen diameter and λ the wavelength. For the large plate aggregate habit only size parameters $x > 3$ are shown, because for smaller sizes it is practically the same as plate type 1. The extinction matrix elements in Fig. 7 and Fig. 8 are normalized by the extinction cross section K_{tro} for total random orientation of the specific shape. Using Eq. 5 the extinction cross section for total random orientation K_{tro} is

$$K_{tro} = \int_0^{\pi} p_{\beta}(\beta) K_{aro,11}(\theta_{inc}, \beta) \sin \beta d\beta. \quad (26)$$

For the large plate aggregate, we skip the tilt angles $\beta > 90^\circ$ in Fig. 8, because for $\beta > 90^\circ$ the results are the same as for $\beta < 90^\circ$ but mirrored around $\theta_{inc} = 90^\circ$. Due to the mirror symmetry to the x-y plane of the hexagonal plates, the curves shown in Fig. 7 are symmetric relative to $\theta_{inc} = 90^\circ$.

For the plate type 1 habit the effect of orientation and incidence angle results in differences of up to 50% of the $K_{aro,11}$ element compared to total random random orientation, whereas for the large plate aggregate habit the biggest differences

are at maximum about 15%. The biggest differences occur for tilt angles of 0° and 90° when looking from the top/bottom
 440 ($\theta_{inc} = 0^\circ, 180^\circ$) and from the side ($\theta_{inc} = 90^\circ$). Depending on the size parameter, shape and magnitude of the curve change.
 For example, the maximum for the plate type 1 habit occurs at tilt angle $\beta = 0^\circ$ and incidence angles of 0° and 180° for $x \lesssim 1$
 and $x \approx 10$, whereas it occurs at an incidence angle of 90° for $x \approx 3$ and $x \approx 5$. The large plate aggregate habit shows a similar
 behavior albeit with much lower magnitude.

The $K_{aro,21}$ matrix element describes the extinction of the polarization difference between vertical and horizontal polariza-
 445 tion and the $K_{aro,43}$ matrix element the extinction of polarization difference between the $+45^\circ$ and -45° polarization. For
 total random orientation, these matrix elements are zero, which is indicated by the gray line in Fig. 7 and Fig. 8. For the plate
 type 1 habit the $K_{aro,21}$ and the $K_{aro,43}$ matrix element show a strong dependency on the tilt angle and the incidence angle,
 which reduces with increasing size parameter. Except when looking from the top/bottom ($\theta_{inc} = 0^\circ, 180^\circ$) both elements are
 non-zero. For the large plate aggregate habit the $K_{aro,21}$ and the $K_{aro,43}$ matrix element are practically zero showing only
 450 small deviations from zero for $x \gtrsim 3$.

The results for the plate type 1 with $x \approx 1.4$ and tilt angle $\beta = 0^\circ$ agree qualitatively with the results of Adams and Bet-
 tenhausen (2012) for azimuthally randomly oriented hexagonal plates with tilt angle $\beta = 0^\circ$ and a similar size parameter but
 at a different frequency. Adams and Bettenhausen (2012) simulated for microwave frequencies among others the scattering of
 azimuthally randomly oriented hexagonal plates with tilt angle $\beta = 0^\circ$.

455 The asymmetry parameter describes the distribution between forward scattering and backscattering and gives an overview
 of the scattering behavior. For example, $g = 0$ means forward scattering and backscattering are of equal strength, whereas
 $g = 1$ and $g = -1$ mean only forward scattering and only backscattering, respectively. The asymmetry parameter for azimuthal
 random orientation is

$$g_{aro}(\theta_{inc}, \beta) = \frac{1}{2} \int_0^{2\pi} \int_0^\pi \cos(\theta_s - \theta_{inc}) Z_{aro,11}(\theta_{inc}, \theta_s, 0, \phi_s, \beta) d\phi_s d\theta_s \quad (27)$$

460 with $Z_{aro,11}$ being the (1, 1)-element of the scattering matrix Z_{aro} . The asymmetry parameter is shown in Fig. 7 and Fig. 8.
 The asymmetry parameters for the different tilt angles are centered around the asymmetry parameter g_{tro} for total random ori-
 entation, which is shown as a gray line. The asymmetry parameter g_{tro} for total random orientation is calculated by integrating
 $g_{aro}(\theta_{inc}, \beta)$ over the tilt angle β similar to Eq. 26. For $x \ll 1$, the total random orientation asymmetry parameter g_{tro} is zero
 indicating symmetric forward and backward scattering as expected for Rayleigh scattering. With increasing size parameter
 465 forward scattering increases. The azimuthal random orientation asymmetry parameter g_{aro} for the large plate aggregate habit
 deviates slightly from the total random orientation asymmetry parameter g_{tro} with changing tilt angle β , whereas for the plate
 type 1 habit it deviates strongly from the total random orientation asymmetry parameter g_{tro} especially for $1 < x < 6$. For
 example, at tilt angle $\beta = 0^\circ$ and incidence angles of 0° and 180° for $x = 1.4$ the scattering in forward and backward direction
 is almost symmetric but at tilt angle $\beta = 90^\circ$ the scattering in forward direction is much stronger than in backward direction.

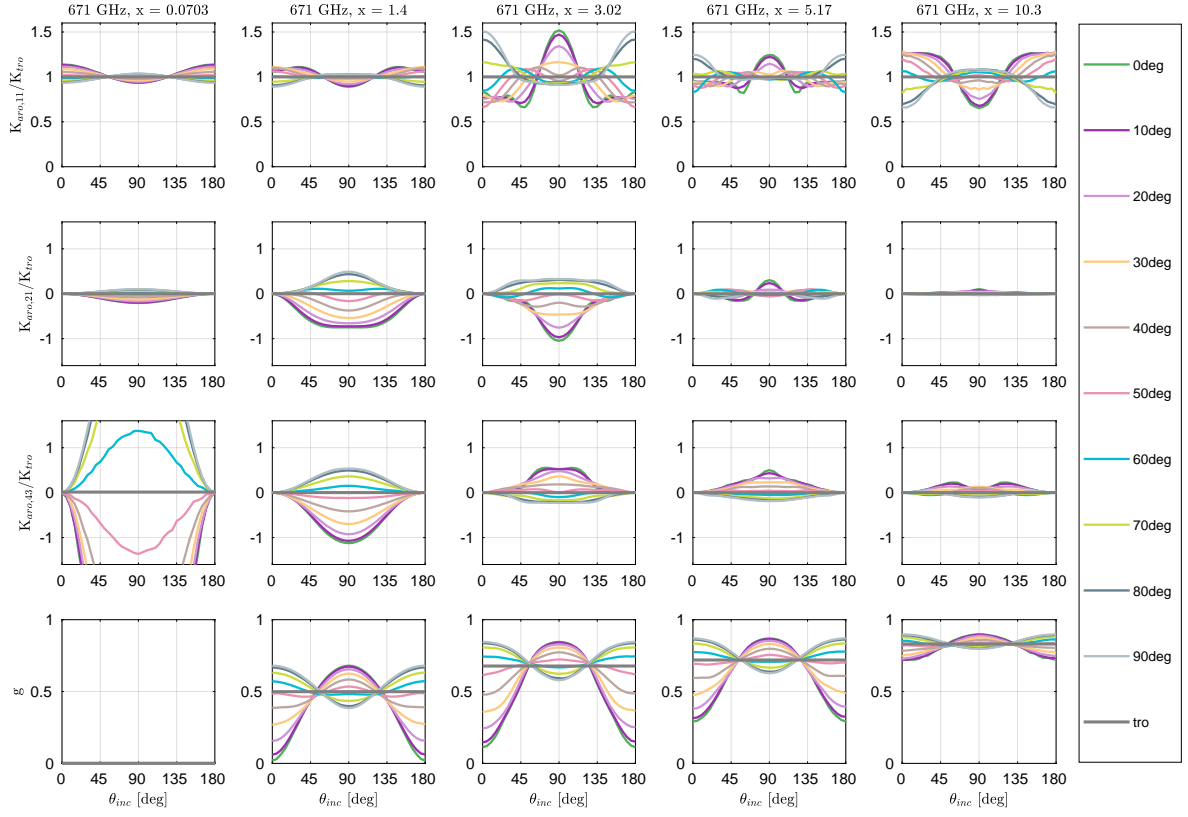


Figure 7. Extinction matrix elements $K_{aro,ij}$ normalized by the extinction cross section for total random orientation and the asymmetry parameter g of plate type 1 (hexagonal plate) for different size parameter x at 671 GHz as function of incidence angle θ_{inc} for several tilt angles β . The gray lines denote total random orientation. The shapes of the scatterers are shown in Fig. 4.

470 5.2 Scattering matrix

The scattering matrix of a particle describes the angular distribution of the scattered radiation in relation to the incidence direction of the incoming radiation. For unpolarized incoming radiation, the Z_{j1} -element with $j = \{1, \dots, 4\}$ ~~show~~ shows the angular distribution of the scattered radiation field. For example, the Z_{11} -element shows the angular distribution of the scattered intensity (I component of the Stokes vector), whereas the Z_{21} -element shows how and where the scattered radiation is horizontally and vertically polarized (Q component of the Stokes vector) due to the scattering. Negative Z_{21} values mean that the horizontal polarization dominates and vice versa. For polarized radiation, the j -th component of the scattered radiation field depends additionally on the coupling with the other components of the incoming Stokes vector, which is described by the Z_{ji} -element with $i = \{2, 3, 4\}$.

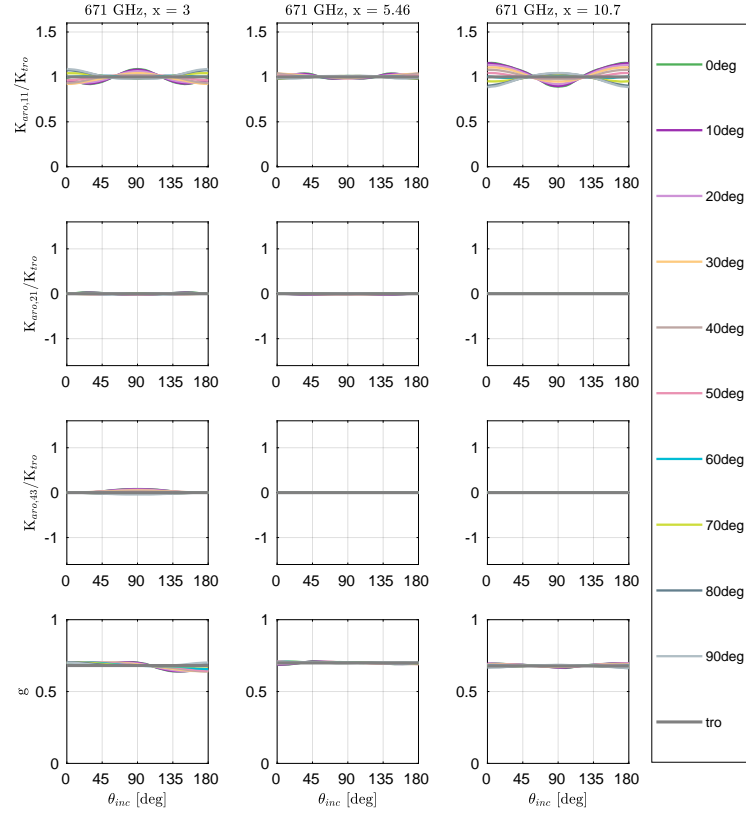


Figure 8. Extinction matrix elements $K_{aro,ij}$ normalized by the extinction cross section for total random orientation and the asymmetry parameter g of large plate aggregate (hexagonal plate aggregate) for different size parameter x at 671 GHz as function of incidence angle θ_{inc} for several tilt angles β . The gray lines denote total random orientation. The shapes of the scatterers are shown in Fig. 4.

After the orientation averaging, the resulting scattering properties possess a rotational symmetry relative to the laboratory z-
 480 axis. The scattering matrix \mathbf{Z}_{aro} (Eqn. 19, D1) depends for tilt angle β on the polar incidence angle θ_{inc} , the polar scattering angle θ_s and the scattering azimuth angle ϕ_s . In contrast, the scattering matrix of totally randomly oriented particles depends only on the scattering angle Θ . The different tilt angles β result in different effective shapes and therefore different scattering matrices. The impact of the tilt angle β depends also on the incidence direction and is different for the different scattering matrix elements.

485 As an example, Fig. 9 shows at 671 GHz and for several incidence angles θ_{inc} and tilt angles β the upper left block of the normalized scattering matrix $\hat{\mathbf{Z}}_{aro}(\theta_{inc}, \theta_s, \phi_s)$ of plate type 1 for size parameter $x \approx 3$. The normalized scattering matrix

$\hat{\mathbf{Z}}_{\text{aro}}(\theta_{\text{inc}}, \theta_s, \phi_s)$ is

$$\hat{\mathbf{Z}}_{\text{aro}}(\theta_{\text{inc}}, \theta_s, \phi_s) = 4\pi \frac{\mathbf{Z}_{\text{aro}}}{\int_0^{2\pi} \int_0^\pi \mathbf{Z}_{\text{aro}}(\theta_{\text{inc}}, \theta_s, \phi_s) d\phi_s d\theta_s}. \quad (28)$$

We show only the upper left block, because these are the most relevant entries of the scattering matrix considering the present
 490 spaceborne microwave and submillimeter wave sensors, but all 16 elements are calculated. At incidence direction $\theta_{\text{inc}} = 0^\circ$,
 the \hat{Z}_{11} - and \hat{Z}_{22} -element differ strongly between the different tilt angles β . Especially in the backscattering direction they
 strongly decrease with increasing tilt angle β . The \hat{Z}_{21} - and \hat{Z}_{12} -element show only slight differences between the different
 tilt angles. Whereas the \hat{Z}_{11} -element decreases at backscattering direction with increasing tilt angle, it is fairly constant at the
 forward direction resulting in total in an increased forward direction, which is also shown by the asymmetry parameter g_{aro}
 495 in Fig. 7. Within the Rayleigh regime ($x \ll 1$, not shown) the influence of the tilt angle β on the normalized scattering matrix
 $\hat{\mathbf{Z}}_{\text{aro}}$ is negligible at incidence direction $\theta_{\text{inc}} = 0^\circ$.

For non nadir/zenith incidence directions the \hat{Z}_{21} - and \hat{Z}_{12} - element as well the other scattering matrix elements differ
 strongly for different tilt angle β . For example, the \hat{Z}_{21} - and \hat{Z}_{12} - elements have a negative peak at $\theta_s = 180^\circ - \theta_{\text{inc}}$ and
 $\phi_s = 0^\circ$ for tilt angle $\beta = 0^\circ$, which means that incoming unpolarized radiation scattered at this direction is horizontally
 500 polarized. There is no peak at this scattering direction for tilt angle ~~$\beta = 30^\circ$~~ $\beta = 50^\circ$ or $\beta = 90^\circ$. For tilt angle ~~$\beta = 30^\circ$~~
 $\beta = 50^\circ$ there is a negative peak at $\theta_s = \theta_{\text{inc}}$ and for tilt angle $\beta = 90^\circ$ there is a positive peak at $\theta_s = \theta_{\text{inc}}$. The negative
 peaks of the \hat{Z}_{21} - and \hat{Z}_{12} - element at $\theta_s = 180^\circ - \theta_{\text{inc}}$ and $\phi_s = 0^\circ$ for $\beta = 0^\circ$ are accompanied by peaks of the \hat{Z}_{11} - and
 \hat{Z}_{22} -element. For tilt angle ~~$\beta = 30^\circ$~~ $\beta = 50^\circ$ or $\beta = 90^\circ$ the \hat{Z}_{11} - and \hat{Z}_{22} -elements do not have peaks at that direction but
 only in the forward direction $\theta_s = \theta_{\text{inc}}$. The peak at $\theta_s = 180^\circ - \theta_{\text{inc}}$ and $\phi_s = 0^\circ$ for tilt angle $\beta = 0^\circ$ coincides with the
 505 specular reflection direction of a plane. The results of Adams and Bettenhausen (2012) for the \hat{Z}_{11} - and the \hat{Z}_{21} - element for
 size parameter $x \approx 4$ fit qualitatively with the \hat{Z}_{11} - and the \hat{Z}_{21} -element for tilt angle $\beta = 0^\circ$ in Fig. 9. Interestingly, the large
 plate aggregate in Fig. 10 with similar size parameter x as the plate type 1 habit in Fig. 9 does not show these peaks. There
 is also no strong backscattering for nadir incidence direction. Fig. 10 shows at 671 GHz and for several incidence angles θ_{inc}
 and tilt angles β the upper left block of the normalized scattering matrix $\hat{\mathbf{Z}}_{\text{aro}}(\theta_{\text{inc}}, \theta_s, \phi_s)$ of large plate aggregate for size
 510 parameter $x \approx 3$. Compared to the plate type 1 habit in Fig. 9 the \hat{Z}_{21} - and \hat{Z}_{12} -elements are practically zero. This means
 unpolarized incoming radiation scattered by the large plate aggregate does not show much polarization. On the other hand, at
 167 GHz the \hat{Z}_{21} - and \hat{Z}_{12} -elements are ~~non-zero~~ ~~non-zero~~ and significantly differ between the different tilt angles β . Fig. 11
 shows at 167 GHz and for several incidence angles θ_{inc} and tilt angles β the upper left block of the normalized scattering matrix
 $\hat{\mathbf{Z}}_{\text{aro}}(\theta_{\text{inc}}, \theta_s, \phi_s)$ of the same large plate aggregate as in Fig. 10. At 167 GHz the size parameter for this particle is $x \approx 0.75$.
 515 Compared to Fig. 10 the scattering is less focused toward the forward scattering direction.

The data from the simulated scattering matrix can be used for simulations of passive and active observations. However, for
 simulations of horizontally scanning radars the scattering matrix in the backscattering direction has to be handled with care.
 In the spherical harmonics representation of the Mueller matrix, the polarization at the poles, which are in the forward and
 backward direction, is not well represented. This can result in errors for the polarization. Most of this is averaged out due to the

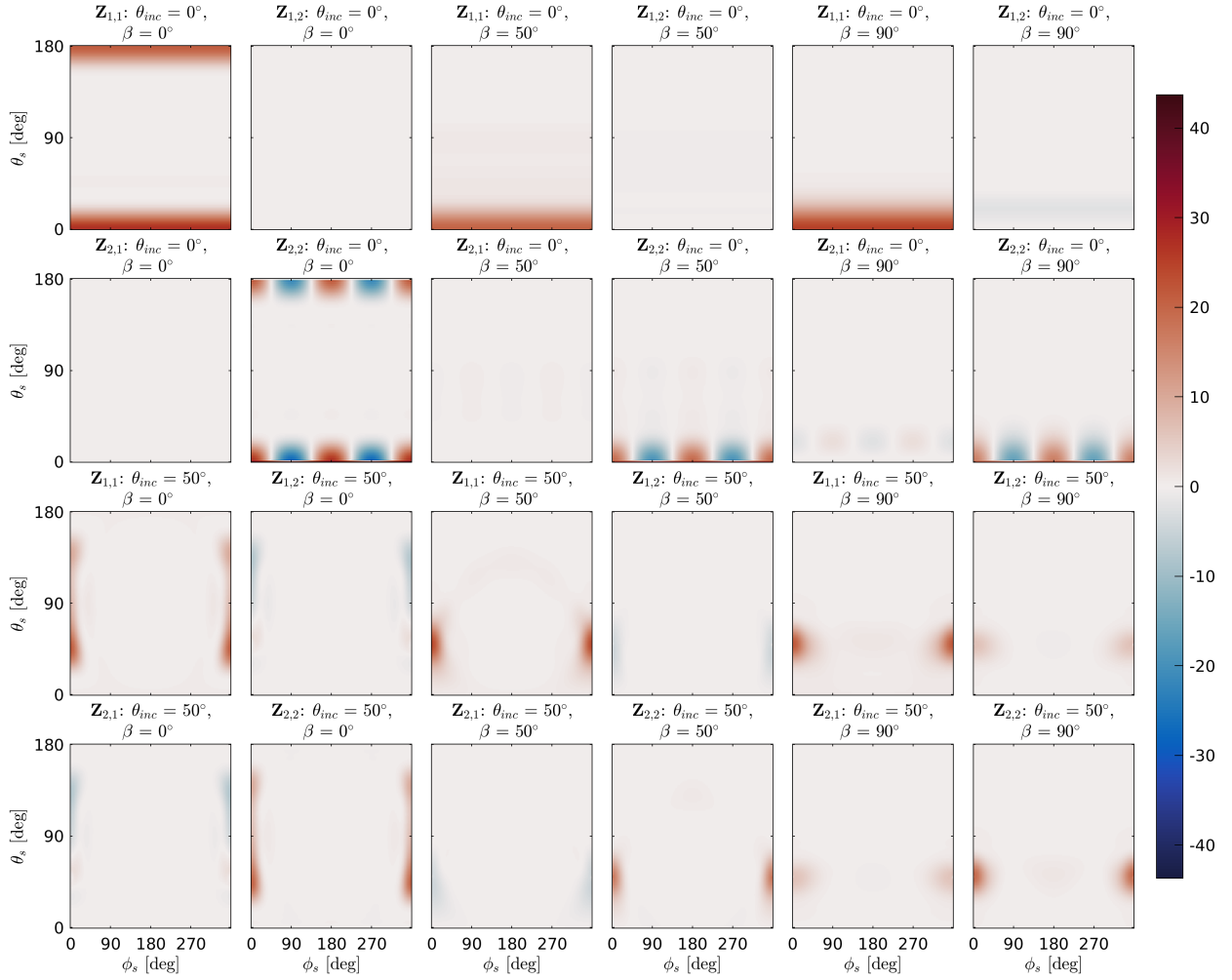


Figure 9. The upper left block of the normalized scattering matrix $\hat{\mathbf{Z}}$ of plate type 1 with a volume equivalent diameter of $429\mu\text{m}$ (Fig. 4) and a size parameter $x \approx 3$ at 671 GHz as function of the polar scattering angle θ_s and the azimuth scattering angle ϕ_s for a set of tilt angles β and incidence angles θ_{inc} .

520 orientation averaging and the transformation to the scattering matrix, but there can be some residual effects for the polarization at the backscattering direction. This will be revised for the next iteration of the database.

6 Radiative transfer simulations

In this section, we show radiative transfer simulations at 166 GHz using azimuthally randomly oriented scatterers in order to give an example of the capabilities of the simulated scattering data. For the radiative transfer simulations, 200 atmospheric profiles over the tropical pacific were taken from one of the EarthCARE scenes. These scenes were prepared for the EarthCARE

525

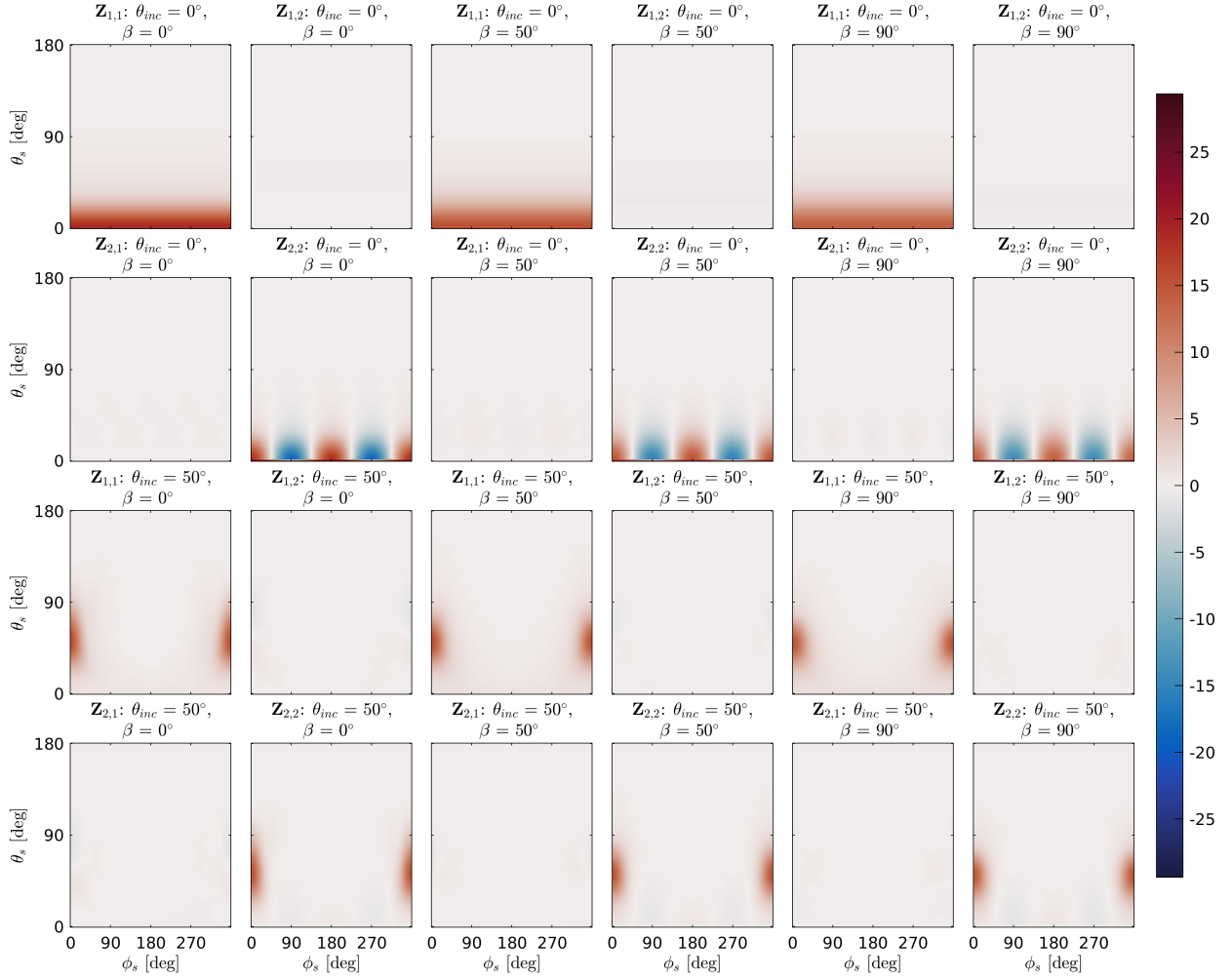


Figure 10. The upper left block of the normalized scattering matrix $\hat{\mathbf{Z}}$ of large plate aggregate with a volume equivalent diameter of $427\ \mu\text{m}$ (Fig. 4) and a size parameter $x \approx 3$ at 671 GHz as function of the polar scattering angle θ_s and the azimuth scattering angle ϕ_s for a set of tilt angles β and incidence angles θ_{inc} .

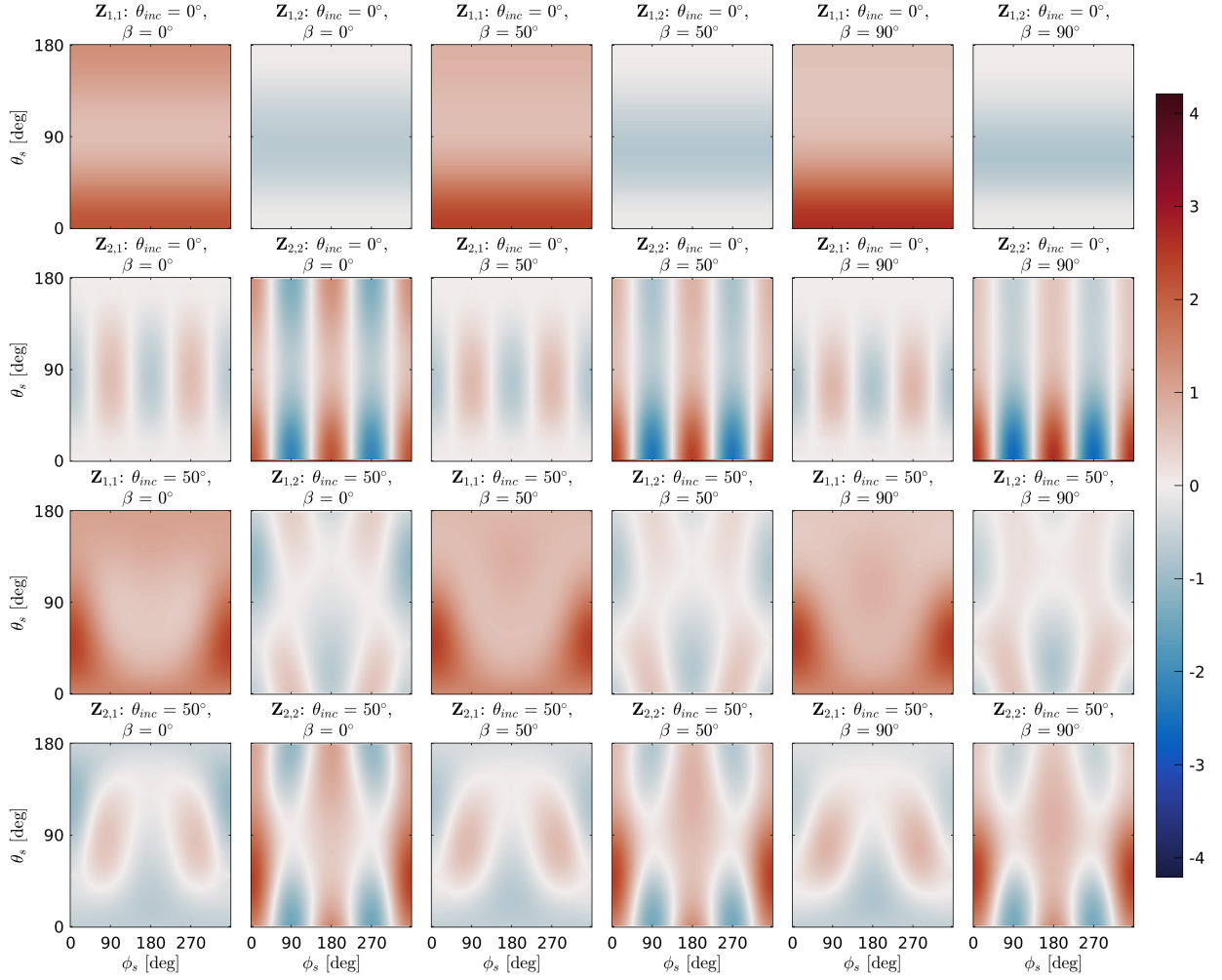


Figure 11. The upper left block of the normalized scattering matrix $\hat{\mathbf{Z}}$ of large plate aggregate with a volume equivalent diameter of $427\ \mu\text{m}$ (Fig. 4) and a size parameter $x \approx 0.75$ at 167 GHz as function of the polar scattering angle θ_s and the azimuth scattering angle ϕ_s for a set of tilt angles β and incidence angles θ_{inc} .

mission with Environment Canada’s high-resolution numerical weather prediction model known as the Global Environmental Multiscale Model (GEM, Côté et al., 1998). The GEM scenes have a resolution of 250m and include two liquid hydrometeor species (rain, liquid clouds) and four frozen hydrometeor species (cloud ice, snow, graupel, and hail). The profiles were randomly selected except for that they should cover the whole possible brightness temperature space as uniformly as possible.

530 The simulations were done using the Atmospheric Radiative Transfer Simulator (ARTS, Buehler et al., 2018; Eriksson et al., 2011) version 2.3.1118. The discrete ordinate iterative solver (DOIT, Emde, 2004) was used as scattering solver within ARTS. The simulations of Rayleigh–Jeans brightness temperatures were done using independent pixel approximation (IPA) with a local incidence angle of 49° for a satellite orbit height of 407 km at ~~164.1 GHz~~ 165.1 GHz and 166.9 GHz, which were averaged to mimic the GMI’s 166 GHz channel. Within ARTS, gas absorption was taken into account by using the HITRAN
535 data base (Rothman et al., 2013) and the MT_CKD model for the continuum absorption of water vapor and molecular nitrogen in version 2.52 (Mlawer et al., 2012). The gas absorption of molecular oxygen was processed by using the full absorption model of Rosenkranz (1998) modified by the values from Tretyakov et al. (2005). The ocean surface emissivity was calculated with the Tool to Estimate Sea-Surface Emissivity from Microwaves to sub-Millimeter waves (TESSEM2, Prigent et al. (2017)) implementation within ARTS using the surface speed and temperature from the GEM profiles.

540 The Milbrandt-Yau two-moment microphysics (Milbrandt and Yau, 2005a, b) implementation within ARTS with the same hydrometeor types and size distributions as for the GEM runs was used. The Milbrandt-Yau two-moment microphysics assumes a modified gamma distribution with characteristic parameters for each individual hydrometeor;

$$N(x) = N_0 x^\nu \exp(-\lambda x^\mu) \quad (29)$$

with the parameters N_0 and λ , which are functions of the number density and the hydrometeor content and parameters μ and ν .
545 The parameters μ and ν are fixed for each hydrometeor type and are summarized in Table 3. The Milbrandt-Yau two-moment bulk microphysics use the particle maximum diameter as independent variable x for the size distribution.

The scattering properties for the hydrometeors were taken from Eriksson et al. (2018) except for cloud ice and snow. The database of Eriksson et al. (2018) contains among others the single scattering properties of hydrometeors, which are modeled to be consistent with the m-D parameters of the Milbrandt-Yau two-moment bulk microphysics scheme. The particles inside
550 the database of Eriksson et al. (2018) are assumed to be totally randomly oriented.

For cloud ice and snow the azimuthally randomly oriented plate type 1 and the azimuthally randomly oriented large plate aggregate are used. No averaging of the scattering data of the particles with its mirrored version was done for the radiative transfer simulation. Normally, this is done to assure that the scattering medium, in our case ice clouds, are mirror symmetric to the incidence plane. Mirrorsymmetric particles like the plate type 1 automatically fulfill this, but unsymmetric particles like the large plate aggregate generally do not. Due to the orientation averaging and the random structure of the large plate aggregate the effect of the non-mirror symmetry are so small, that we neglected it for the radiative transfer simulations. For the simulations the azimuthally randomly oriented particles are orientation-averaged over Gaussian distributed β angles with zero mean and increasing standard deviation. ~~6~~ Six different orientation states were prepared for the simulations to mimic different stages of

Table 3. Size distribution parameters and the scatterer shape of the radiative transfer simulations. The size distribution parameters were taken from the source code of the Milbrandt-Yau two-moment bulk microphysics (Milbrandt and Yau, 2005a, b) of the GEM model. Except for cloud ice and snow the scattering properties were taken from Eriksson et al. (2018).

	MGD parameter		scatterer habits		
	ν	μ	Fig. 12	Fig. 13	Fig. 15
cloud water	1	1	Liquid Sphere, ID 25	Liquid Sphere, ID 25	Liquid Sphere, ID 25
rain	0	1	Liquid Sphere, ID 25	Liquid Sphere, ID 25	Liquid Sphere, ID 25
cloud ice	0	1	Plate Type 1 (ARO)	Plate Type 1 (ARO)	Plate Type 1 (ARO)
snow	0	1	Large plate aggr. (ARO)	Large plate aggr. (ARO)	Plate Type 1 (ARO)
graupel	0	1	GEM Graupel, ID 33	-	GEM Graupel, ID 33
hail	0	1	GEM Hail, ID 34	GEM Hail, ID 34	GEM Hail, ID 34

fluttering of the particle. Additionally, the azimuthally randomly oriented particles were averaged over uniformly distributed β angle to show the results for total random orientation. The used single scattering properties are summarized in Table 3.

6.1 Results and discussion

Fig. 12 shows the vertical polarization of the brightness temperature T_{bv} and the polarization difference $T_{bv} - T_{bh}$ as function of the frozen water path (FWP) for the different orientations. The FWP is the sum of each vertically integrated mass content of the four frozen hydrometeors. The plate type 1 habit for ice clouds and the large plate aggregate habit for snow were used for the simulation, see Table 3 for the other hydrometeors. The vertical polarization of the brightness temperature T_{bv} decreases from ≈ 280 K at a FWP of $\approx 10^{-2}$ kg m $^{-2}$ with increasing frozen water path to ≈ 85 K at a FWP of ≈ 20 kg m $^{-2}$. The polarization difference $T_{bv} - T_{bh}$ increases with increasing FWP till a maximum is reached at a FWP of ≈ 5 kg m $^{-2}$ and then decreases with increasing FWP. The maximum of the polarization difference depends on the orientation state. For total horizontal orientation the maximum polarization difference is ≈ 11 K. With increased standard deviation (fluttering) the maximum polarization difference decreases down to ≈ 2.5 K for totally randomly oriented particles. The orientation depending polarization difference also indicates that particle orientation is not only an issue for dual polarized observations but also for single polarized observations. Ignoring orientation can cause a negative bias for vertically polarized observations and in a positive bias for horizontally polarized observations.

Additionally, Fig. 12 shows the polarization difference $T_{bv} - T_{bh}$ as function of the vertical polarized brightness temperature T_{bv} . The polarization difference has a bell like-shaped distribution with a flat top and its maximum at ≈ 195 K for total horizontal orientation. With increased standard deviation the curve gets flatter. For small standard deviations ($\leq 10^\circ$) the bell like distributions of the polarization difference are similar to the mean polarization differences that Gong and Wu (2017) estimated from GMI measurements over tropical ocean and the mean polarization differences that Defer et al. (2014) estimated from MADRAS. The results of Gong and Wu (2017) and of Defer et al. (2014) are additionally additionally shown in Fig. 12

580 as gray solid and dashed lines. Though MADRAS has a slightly higher incidence angle than GMI and measures at 157GHz instead of 166 GHz, the observations of GMI and MADRAS are similar.

Additional tests show that the polarization difference and the brightness temperature are mainly influenced by snow and graupel. For these tests (not shown) one hydrometeor at a time was set to zero, while the others were unchanged, and the simulations for the 200 profiles and 7 orientation states were rerun. Cloud liquid and rain have [an](#) impact on single profiles but
585 do not change the overall behavior of the polarization difference. The influence of ice clouds is negligible, because most of the ice cloud particles are too small to cause significant scattering at 166 GHz. Hail does not need to be considered, because within the 200 profiles its content is very little and therefore does not cause any significant scattering. Setting graupel or snow to zero strongly alters the polarization difference and the brightness temperature.

For the simulations shown in Fig. 13 the mass content and number density of graupel was added to snow but without
590 changing the total amount of frozen water mass content and the other hydrometeors. In this case snow is the only significant cause of scattering. Compared to Fig. 12 the minimum brightness temperature T_{bv} is higher by ≈ 40 K, which means that the scattering of the large plate aggregate habit is weaker than the graupel habit. The reason for that is that the graupel habit due to its higher density has a larger scattering coefficient than the large plate aggregate. More interesting is how the polarization differs. The polarization difference $T_{bv} - T_{bh}$ distribution has indications of a bell like distribution but compared to Fig. 12
595 it does not reach zero for the minimum brightness temperature T_{bv} and it is flatter. Furthermore, the polarization difference maximum is shifted by ≈ 30 K to lower brightness temperature and is slightly higher. Down to $T_{bv} \approx 170$ K the polarization differences for small standard deviations ($\leq 10^\circ$) are similar to the observed ~~polarization~~[polarization](#) differences of Gong and Wu (2017) and of Defer et al. (2014). For $T_{bv} \lesssim 170$ K the polarization differences are larger than the observed ones. Around brightness temperature $T_{bv} = 125$ K, approximately the minimum brightness temperature, the polarization difference is roughly
600 twice as [large as](#) for the similar brightness temperature in Fig. 12 and the observations of Gong and Wu (2017) and of Defer et al. (2014).

The bell like distribution of the polarization difference $T_{bv} - T_{bh}$ in Fig. 13 is caused by two opposing effects. On one hand increasing the amount of scatterers results in increased scattering and in increased polarization difference. On the other hand, increasing the amount of scatterers results in increased multi-scattering and in decreased polarization difference. For small
605 amount of scattering the polarization increase dominates and for large amount of scattering polarization decrease dominates.

In Fig. 13 snow is the only significant cause of scattering, whereas in Fig. 12 snow and graupel are the causes of scattering. The smaller polarization differences in Fig. 12 compared to Fig. 13 for brightness temperatures $T_{bv} < 220$ K show that not only multi-scattering reduces the polarization but also the composition of the scatterers. As the amount of frozen particles increases the composition changes. For small amount of frozen hydrometeors the amount of snow dominates whereas the
610 amount of graupel dominates for large amount of frozen hydrometeors, see Fig. 14. Graupel is simulated by the GEM graupel habit of the database of Eriksson et al. (2018). Due to its total random orientation and its ~~sphere-like~~[sphere-like](#) shape the GEM graupel habit causes only negligible polarization at 166 GHz. For small amount of frozen hydrometeors snow dominates the scattering and increasing the amount of frozen hydrometeors results in increased scattering and in increased polarization difference. With increasing amount of frozen hydrometeors not only multi-scattering increases but also the scattering due to

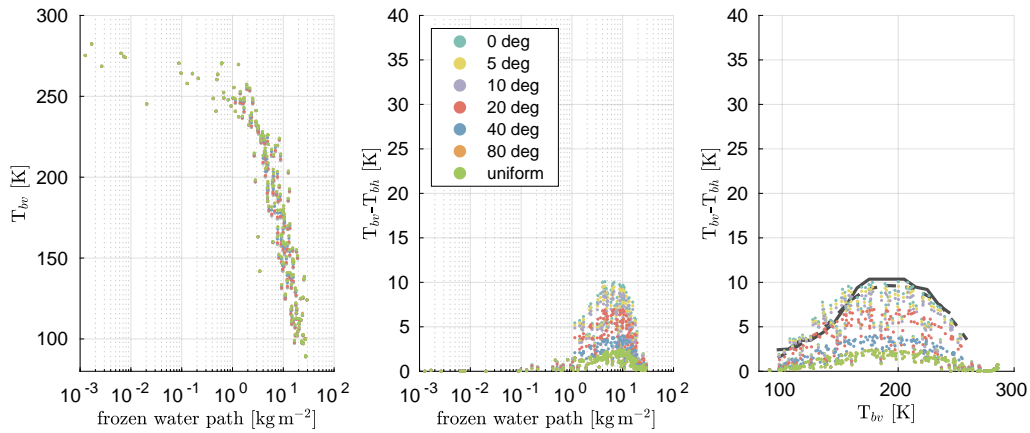


Figure 12. Simulated brightness temperature at 166 GHz for 200 randomly selected atmospheric profiles. For each of these atmospheric profiles the scattering properties of the azimuthally randomly oriented scatterers are orientation averaged over 7 different distributed β angles with zero mean and different standard deviation. The different colors denote the standard deviation of the β angle distribution and the distribution type. For the used scatterers, see Table 3. The gray line solid line denotes the mean polarization difference over tropical ocean from GMI observations at 166 GHz of Gong and Wu (2017) and the gray dashed line the mean polarization difference over tropical ocean from MADRAS observations at 157 GHz of Defer et al. (2014).

615 graupel. Both decreases the polarization difference. Due to this the polarization difference in Fig. 12 is smaller for $T_{bv} < 220$ K and the maximum polarization difference is at higher brightness temperatures than in Fig. 13.

As an additional scenario, the large plate aggregate habit for snow was replaced by the plate type 1 habit and the simulations for the 200 profiles and 7 orientation states were rerun, which is shown in Fig. 15. The polarization difference $T_{bv} - T_{bh}$ distribution has similar shape as in Fig. 12 but it has a roughly three times higher magnitude and a much higher spread, 620 whereas the brightness temperature T_{bv} differs only slightly. This shows that the polarization difference not only depends on the orientation but on the shape, too. For a standard deviation of $\approx 40^\circ$ the bell like distribution of the polarization difference is comparable to the mean polarization differences of Gong and Wu (2017) and of Defer et al. (2014).

The comparison of the three different scenarios with the observations of Gong and Wu (2017) and of Defer et al. (2014) shows that snow simulated as large plate aggregate with small standard deviations ($\leq 10^\circ$) or as plate type 1 with standard 625 deviations in the order of $\mathcal{O}(40^\circ)$ is compatible with the observations, if additionally graupel is included within the simulations. Without graupel, the observed decrease of the polarization differences for brightness temperature $T_{bv} < 170$ K cannot be reached.

7 Summary

We provide microwave and submillimeter wave scattering simulations of azimuthally randomly oriented ice crystals with a 630 fixed but arbitrary tilt angle. For the simulations, DDA simulations made with ADDA were combined with a self developed

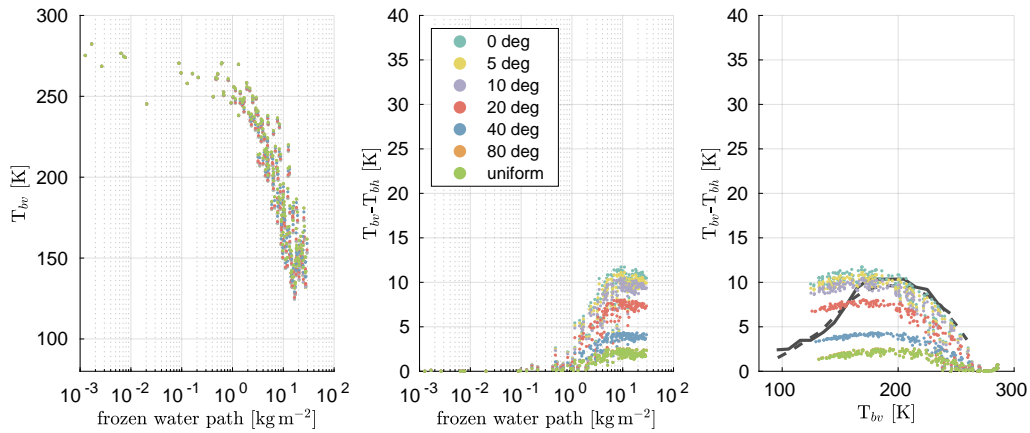


Figure 13. Same as Fig. 12 but the mass content and the number density of graupel added to snow.

orientation averaging approach. The scattering of 51 sizes of hexagonal plates (plate type 1) between $10\mu\text{m}$ and $2,596\mu\text{m}$ volume equivalent diameter and 18 sizes of hexagonal plate aggregates (large plate aggregate) between $197\mu\text{m}$ and $4,563\mu\text{m}$ for 35 frequencies between 1 GHz and 864 GHz and 3 temperatures (190 K, 230 K, 270 K) were simulated. The scattering data for azimuthal random orientation is much more complex than for total random orientation. Whereas for total random orientation the scattering matrix $\mathbf{Z}_{tro}(\Theta)$ depends only on one angle and the extinction matrix \mathbf{K}_{tro} has no angular dependency at all and has only one independent entry, for azimuthal random orientation the scattering matrix $\mathbf{Z}_{aro}(\theta_{inc}, \theta_s, \phi_s)$ depends on three angles and the extinction matrix $\mathbf{K}_{aro}(\theta_{inc})$ depends on the incidence angle and has three independent entries. Furthermore, the tilt angle β **adds an additional dimension** increases the complexity. Due to the high demands in view of computation time and the amount of data we have to compromise in terms of the accuracy of the resulting scattering data, which is in the order of a few percent. For a finite set of incidences and tilt angles, in which the incidence angles θ_{inc} span a range from 0° to 180° with a 5° spacing and the tilt angles β span a range from 0° to 90° for plate type 1 and from 0° to 180° for large plate aggregates with a 10° spacing, the scattering data has a size of 181 GB, which is roughly 20 times bigger than the **whole** database of Eriksson et al. (2018). The scattering database of the azimuthally randomly oriented particles is publicly available from Zenodo (<https://doi.org/10.5281/zenodo.3463003>). The scattering database is organized so that the Python 3 interface of the database of Eriksson et al. (2018) can be used to extract and interact with the data.

To give an example of the capabilities of the dataset, we conducted radiative transfer simulations of polarized GMI measurements of differently fluttering ice crystals at 166 GHz. The radiative transfer simulations were conducted using ARTS (Buehler et al., 2018; Eriksson et al., 2011) and assuming Milbrandt-Yau two-moment microphysics (Milbrandt and Yau, 2005a, b) with two liquid hydrometeor species (rain, liquid clouds) and four frozen hydrometeor species (cloud ice, snow, graupel, and hail). For slightly fluttering snow and ice particles, the simulations show polarization differences up to 11 K using the azimuthally randomly oriented large plate aggregate habit for snow, the plate type 1 habit for cloud ice and totally oriented particles for the other four hydrometeors. The simulations cover the observed brightness temperatures and polarization differences from Gong

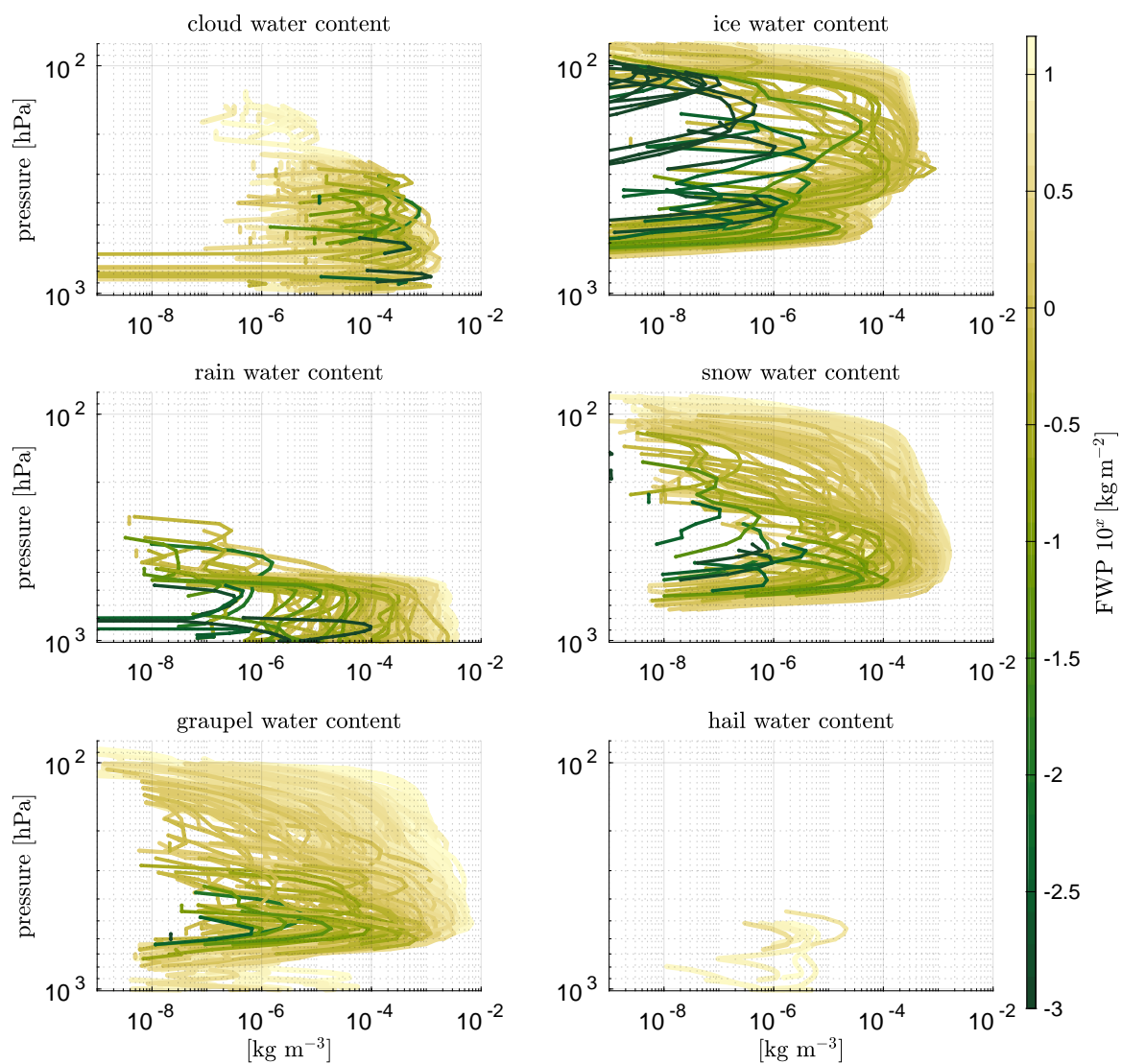


Figure 14. Hydrometeor content profiles used for the radiative transfer simulation in Fig. 12. The color indicates the frozen water path (FWP) of each atmospheric profile.

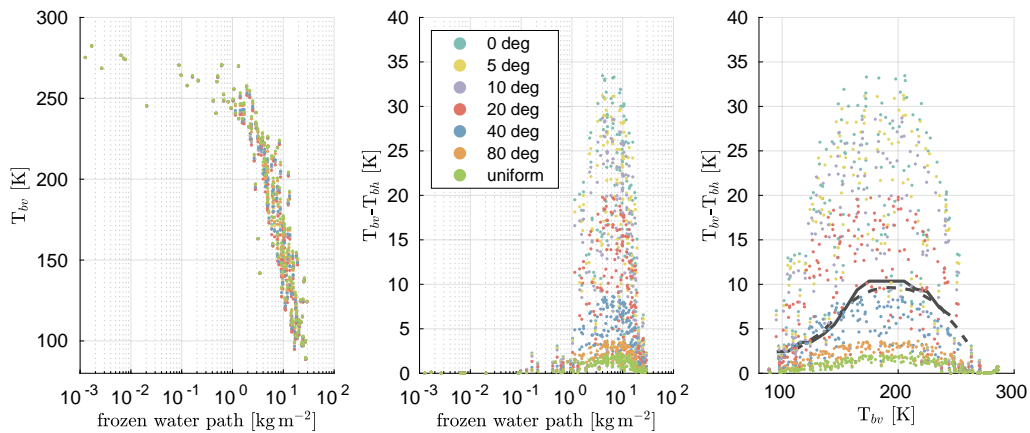


Figure 15. Same as Fig. 12 but with plate type 1 for snow instead of large plate aggregate.

and Wu (2017) and Defer et al. (2014). Further analysis shows that not only multi-scattering affects the polarization but also the hydrometeor composition. The polarization difference and the brightness temperature are mainly influenced by snow and
 655 graupel. Exchanging the large plate aggregate habit with the plate type 1 habit for snow results in roughly three times bigger polarization difference. For strongly fluttering snow and ice particles, the simulations using the plate type 1 habit for snow and ice are similar to Gong and Wu (2017) and Defer et al. (2014). Particle orientation also affects single polarized observations. Ignoring orientation can cause a negative bias for vertically polarized observations and in a positive bias for horizontally polarized observations.

660 Using the new scattering data for retrievals of polarized observations from GMI, MADRAS and especially the upcoming ICI can give us new insights for the understanding of clouds. For example, to the authors' knowledge none of the latest atmospheric weather and climate models handle orientation. Furthermore, polarization can give us additional ~~informations~~ information on the shape of the particle.

Data availability. The scattering database of the azimuthally randomly oriented particles is publicly available from Zenodo (<https://doi.org/10.5281/zenodo.3463003>). The data of the radiative transfer simulations of Sect. 6 is also publicly available from Zenodo (<https://doi.org/10.5281/zenodo.3475897>). [The data from the DDA simulations is available upon request from us.](#)

Competing interests. The authors declare that they have no conflict of interest.

670 *Author contributions.* Manfred Brath has developed the orientation averaging approach, set up and conducted the scattering and the radiative transfer simulations and written the article’s text. Robin Ekelund prepared the scatterer shape data, designed the database structure and contributed text. ~~Patrick Eriksson has acted as project leader and initiated the database.~~ [Patrick Eriksson has acted as project leader, initiated the database and suggested the averaging approach.](#) Patrick Eriksson and Stefan A. Buehler participated in planning of the database and have contributed text. Oliver Lemke helped to set up and to conduct the scattering simulations and prepared the data for publication.

675 *Acknowledgements.* A large part of this work was produced inside a study funded by EUMETSAT (Contract No. EUM/COS/LET/16/879389). The study manager at EUMETSAT was Christophe Accadia, who provided appreciated feedback and inspiration. Robin Ekelund and Patrick Eriksson were further supported financially by the Swedish National Space Agency (SNSA) under grant 150/14. The authors would like to thank Howard Barker from Environment and Climate Change Canada for providing the GEM model simulations. Stefan A. Buehler was supported by the Deutsche Forschungsgemeinschaft (DFG, German Research Foundation) under Germany’s Excellence Strategy — EXC 2037 [“Climate, Climatic Change, and Society”](#) — Project Number: 390683824, contributing to the Center for Earth System Research and Sustainability (CEN) of Universität Hamburg. Finally, our thanks to the ARTS radiative transfer community for their help with using ARTS.

680 **Appendix A: Initial particle alignment**

Before any orientation averaging can be performed, the initial orientation of the particle has to be defined. The alignment algorithm is based mainly on aligning the principal moments of inertia axes along the Cartesian coordinate axes. Also, a number of special cases are treated in order to make the alignment consistent between particles and not dependent on small numerical differences. The result of the algorithm is that the particle fulfills the following criteria: the principal axis of the particle with the largest inertia is aligned along the z-axis, and its principal axis with the smallest inertia along the x-axis.

The algorithm involves a several steps. For particles that possess no symmetries, one step can be skipped. The algorithm operates on a coordinate grid and consists of the following steps:

1. First, the particle mass center coordinate $\underline{\mathbf{r}}_{\mathcal{C}}$ is calculated, according to

$$\underline{\mathbf{r}}_{\mathcal{C}} = \sum_{i=1}^N m_i \underline{\mathbf{r}}_i, \quad (\text{A1})$$

690 where $\underline{\mathbf{r}}_i$ is (3x1) column vector describing the coordinate of the grid point with index i , and m_i is the mass of the corresponding dipole. The dipole grid is then displaced so that the mass center is located at the origin.

2. Next, the inertia matrix $\underline{\mathbf{I}}$ relative to the origin is calculated using

$$\underline{\mathbf{I}} = - \sum_{i=1}^N m_i [\underline{\mathbf{R}}_i]_i [\underline{\mathbf{R}}_i]_i^2, \quad (\text{A2})$$

where $\underline{\mathbf{R}}_i$ is the skew-symmetric matrix associated with coordinate \mathbf{r}_i , defined as

$$\underline{\mathbf{R}} = \begin{pmatrix} 0 & -z & y \\ z & 0 & -x \\ -y & x & 0 \end{pmatrix}. \quad (\text{A3})$$

$\underline{\mathbf{I}}$ contains the products of inertia along the Cartesian coordinate axes, i.e.

$$\underline{\mathbf{I}} = \begin{pmatrix} I_{xx} & I_{xy} & I_{xz} \\ I_{xy} & I_{yy} & I_{yz} \\ I_{xz} & I_{yz} & I_{zz} \end{pmatrix}. \quad (\text{A4})$$

Since $\underline{\mathbf{I}}$ is real and symmetric, it can be diagonalized using eigenvector decomposition, as

$$\underline{\mathbf{\Lambda}} = \underline{\mathbf{Q}} \underline{\mathbf{\Lambda}} \underline{\mathbf{Q}}^T, \quad (\text{A5})$$

where $\underline{\mathbf{\Lambda}}$ is a diagonal matrix with elements I_1 , I_2 and I_3 , which are called the principal moments of inertia. The diagonalization is performed in such way that $I_1 \leq I_2 \leq I_3$. The columns of $\underline{\mathbf{Q}}$, Q_1 , Q_2 and Q_3 , are the corresponding principal axes.

It follows that $\underline{\mathbf{Q}}$ is a rotation matrix, which rotates the x , y and z -axes to corresponding axes of inertia. Thus, to align the particle principal axes to the coordinate axes, one has to rotate the particle grid by the inverse of $\underline{\mathbf{Q}}$, i.e. $\underline{\mathbf{Q}}^T$.

In order to ensure that the rotation does not mirror the particle (that the rotation is pure), one has to make sure that $\det(\underline{\mathbf{Q}}^T) = \det(\underline{\mathbf{Q}}) = 1$. The rotation matrix $\underline{\mathbf{A}}$ is thus calculated as

$$\underline{\mathbf{A}} = \frac{\underline{\mathbf{Q}}^T}{|\underline{\mathbf{Q}}^T|}. \quad (\text{A6})$$

After the rotation, recalculation of the inertia matrix should yield

$$\underline{\mathbf{I}} = \begin{pmatrix} I_{xx} & 0 & 0 \\ 0 & I_{yy} & 0 \\ 0 & 0 & I_{zz} \end{pmatrix}, \quad (\text{A7})$$

With

$$I_{xx} \leq I_{yy} \leq I_{zz}. \quad (\text{A8})$$

This criteria must always be satisfied, i.e. any of the remaining steps must make sure that it does not violate the condition.

3. If the particle contains symmetries, then two or all of the principal moments of inertia can be equal. This means that the rotation in the previous step is unambiguous, i.e. several possible orientations fulfill Eq. A8. As an example, for hexagonal plates, $I_{xx} = I_{yy}$, meaning that its orientation in the xy -plane is unambiguous. It is desirable to remove this uncertainty, which here is done by minimizing the particle dimensions along the coordinate axes. Three cases are possible and are treated as follows:

- 720
- $I_{xx} = I_{yy} = I_{zz}$: The particle is spherically symmetric (for example, a six bullet rosette), hence no rotation will have an impact on \hat{I} . First, the particle dimension along the z-axis is minimized by rotation around the x and y-axis. Similarly, the particle dimension along the x-axis is then maximized by rotation around the z-axis.
 - $I_{yy} = I_{zz}$: The particle is symmetric around the x-axis (a hexagonal column for example). The particle dimension along the z-axis is minimized by rotation around the x-axis.
 - $I_{yy} = I_{xx}$: The particle is symmetric around the z-axis (for example, a hexagonal plate). The particle dimension along the x-axis is maximized by rotation around the z-axis
- 725
4. In the final step, it is determined whether the particle is aligned upside down or upright. First, the minimum circumsphere of the particle is calculated, with its corresponding center. If the center is found to be below the mass-center of the particle (with respect to the z-axis), then the particle is said to be aligned upright. Vice versa, it is said to be aligned upside down in the case when the sphere center is above the mass center. In this case, the particle is rotated 180° around the x-axis to be upright.

730 **Appendix B: Particle rotation**

The key point in our averaging approach is the rotation of the particle for the averaging process. When rotating the particle the wave reference system rotates, too. The wave reference system is the coordinate system that is defined by the incidence direction and the particle system. The changed direction $\hat{e}_{i,rot}$ for a desired orientation is given by

$$\hat{e}_{i,rot} = \mathbf{R}_{\alpha\beta\gamma} \hat{e}_i \quad (\text{B1})$$

735 with \hat{e}_i the non-rotated incidence or scattering direction and $\mathbf{R}_{\alpha\beta\gamma}$ the rotation matrix. The rotation matrix $\mathbf{R}_{\alpha\beta\gamma}$ is

$$\mathbf{R}_{\alpha\beta\gamma} = \mathbf{R}_\alpha(\alpha) \mathbf{R}_\beta(\beta) \mathbf{R}_\gamma(\gamma) = \begin{pmatrix} R_{11} & R_{12} & R_{13} \\ R_{21} & R_{22} & R_{23} \\ R_{31} & R_{32} & R_{33} \end{pmatrix} \quad (\text{B2})$$

with the Euler angles α , β , and γ . The rotation matrix elements R_{ij} are

$$R_{11} = \cos(\gamma) \cos(\beta) \cos(\alpha) - \sin(\gamma) \sin(\alpha) \quad (\text{B3})$$

740 $R_{12} = \cos(\gamma) \cos(\beta) \sin(\alpha) + \sin(\gamma) \cos(\alpha) \quad (\text{B4})$

$$\underline{R_{13}} = -\cos(\gamma) \sin(\beta) \quad (\text{B5})$$

$$\underline{R_{21}} = -\sin(\gamma) \cos(\beta) \cos(\alpha) - \cos(\gamma) \sin(\alpha) \quad (\text{B6})$$

745

$$\underline{R_{22}} = -\sin(\gamma) \cos(\beta) \sin(\alpha) + \cos(\gamma) \cos(\alpha) \quad (\text{B7})$$

$$\underline{R_{23}} = \sin(\gamma) \sin(\beta) \quad (\text{B8})$$

$$750 \quad \underline{R_{31}} = \sin(\beta) \cos(\alpha) \quad (\text{B9})$$

$$\underline{R_{32}} = \sin(\beta) \sin(\alpha) \quad (\text{B10})$$

$$\underline{R_{33}} = \cos(\beta) \quad (\text{B11})$$

755 with Euler angles α , β , and γ (Tsang et al., 2000). When the wave reference system changes, the polarization directions change, too. The polarization directions of each simulated Mueller matrix and extinction matrix are relative to the wave reference system, which is different for each incidence angle. This means the original polarization directions of the Mueller matrix and the extinction matrices change under rotation as indicated in Fig. B1. The rotation about the laboratory Z-axis by the Euler angle α does not change the polarization, because the vertical polarization direction stays always in the plane spanned
 760 by incidence direction unit vector \hat{e}_{ki} and the laboratory z-axis and the horizontal polarization direction stays parallel to the x-y-plane. But the combined rotations by the Euler angles β and γ do change. After the combined rotation the original vertical polarization unit vector \hat{e}_v is rotated out of the plane spanned by incidence direction unit vector \hat{e}_{ki} and the laboratory z-axis by angle φ and original horizontal polarization unit vector \hat{e}_h is rotated out of the x-y-plane by angle φ . After the rotation using $\underline{R}_{\alpha\beta\gamma}$, the polarization of the Mueller matrix \underline{M} and the extinction matrix \underline{K} need to be transformed to the laboratory
 765 polarization using the Stokes rotation matrix \underline{L} (Mishchenko et al., 2002).

$$\underline{L}(\varphi) = \begin{pmatrix} 1 & 0 & 0 & 0 \\ 0 & \cos 2\varphi & -\sin 2\varphi & 0 \\ 0 & \sin 2\varphi & \cos 2\varphi & 0 \\ 0 & 0 & 0 & 1 \end{pmatrix}. \quad (\text{B12})$$

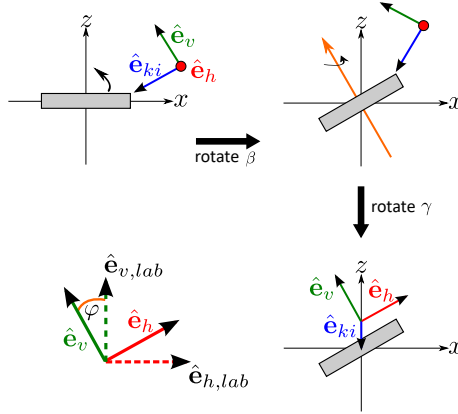


Figure B1. Change of the polarization directions under rotation. (top left) the incidence direction unit vector \hat{e}_{ki} together with the vertical polarization unit vector \hat{e}_v and the horizontal polarization unit vector \hat{e}_h , which are fixed to the particle, before the rotation is performed. (top right) the unit vectors after the rotation by angle β and (bottom right) after the rotation by angle γ . As indicated (bottom left) the polarization vectors after the rotation by angles β and γ are twisted by angle φ compared to the laboratory unit vectors.

The Mueller matrix M_{rot} and the extinction matrix K_{rot} of the rotated particle are given by

$$\underline{M_{rot}} = R_{\alpha\beta\gamma}^*(M) = L(\varphi) M(R_{\alpha\beta\gamma}(\theta_{inc}, \phi_{inc}), R_{\alpha\beta\gamma}(\theta'_s, \phi'_s)) L(-\varphi) \quad (B13)$$

and

$$770 \quad \underline{K_{rot}} = R_{\alpha\beta\gamma}^*(K) = L(\varphi) K(R_{\alpha\beta\gamma}(\theta_{inc}, \phi_{inc})) L(-\varphi). \quad (B14)$$

The rotation angle φ is

$$\underline{\varphi} = \text{atan2}(\hat{e}_v \cdot \hat{e}_{h,lab}, \hat{e}_v \cdot \hat{e}_{v,lab}) \quad (B15)$$

with the rotated vertical polarization direction \hat{e}_v , the horizontal polarization direction in the laboratory system

$$\underline{\hat{e}_{h,lab}} = \hat{e}_{v,lab} \times \hat{e}_{ki}, \quad (B16)$$

775 the vertical polarization direction in the laboratory system

$$\underline{\hat{e}_{v,lab}} = (\hat{e}_z \times \hat{e}_{ki}) \times \hat{e}_{ki}, \quad (B17)$$

and z-direction \hat{e}_z .

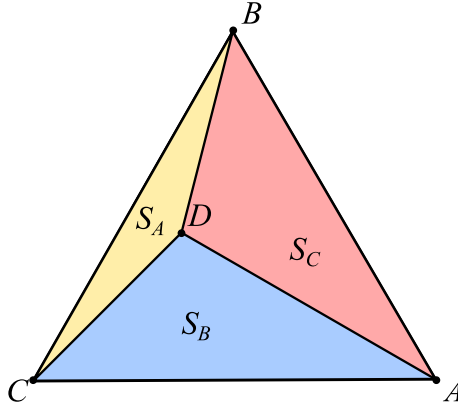


Figure C1. Geometry of triangular barycentric interpolation.

Appendix C: Barycentric interpolation

On an icosahedral grid any arbitrary point on the sphere is accompanied by three nearest points that form an equilateral triangle. Within this triangle the value at that point can be interpolated from the vertices of the triangle. A schematic of the problem is shown in Fig. C1. The vertices A , B , and C form the equilateral triangle ABC . The point D is the evaluation point. Always two vertices and the evaluation point D form a sub-triangle. For example, the vertices B and C and the evaluation D form the triangle BCD on the opposing side of vertex A . The idea behind the barycentric interpolation is to use the ratio of the area of a sub-triangle and the area of the triangle ABC as interpolation weights. The weight belonging to vertex A is

$$w_A = \frac{S_A}{S_{ABC}} \quad (C1)$$

with S_A the area of sub-triangle BCD and S_{ABC} the area of the triangle ABC . The weights belonging to the other two vertices are analogue to the weight of vertex A . The area S of a triangle is using Heron's formula

$$S_i = \sqrt{s(s-u)(s-v)(s-w)} \quad (C2)$$

with

$$s = \frac{u+v+w}{2} \quad (C3)$$

and u, v, w the sides of the triangle i . The interpolated value f_{int} at the evaluation point D is

$$f_{int}(D) = w_A f(A) + w_B f(B) + w_C f(C) \quad (C4)$$

with $f(i)$ the value at a vertex i .

Appendix D: Transformation of the averaged Mueller matrix to the averaged scattering matrix

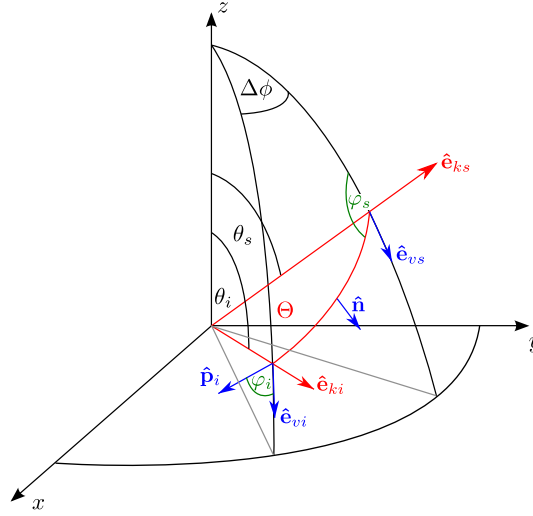


Figure D1. Scattering geometry in the laboratory system

795 Between the scattering matrix averaged Z and the averaged Mueller matrix M following relationship holds

$$\underline{Z}(\theta_{inc}, \theta_s, \phi_s, \beta) = \frac{1}{k^2} \underline{L}(-\varphi_s) \underline{M}(\theta_{inc}, R(\theta'_s, \phi'_s), \beta) \underline{L}(\varphi_i) \quad (D1)$$

with k the angular wavenumber, \underline{L} the Stokes rotation matrix (Eq. B12), φ_i, φ_s the polarization rotation angles, and $R(\theta'_s, \phi'_s)$ the rotation operator that transforms the incidence direction related coordinate system to the laboratory system.

800 As defined in Sect. 2.2, the incidence azimuth direction is zero. In that case the incidence direction vector is always within the X-Z-plane. The rotation operator $R(\theta'_s, \phi'_s)$ then is

$$\begin{pmatrix} \theta_s \\ \phi_s \end{pmatrix} = R \begin{pmatrix} \theta'_s \\ \phi'_s \end{pmatrix} = \begin{pmatrix} \arccos(-\sin \theta_{inc} \sin \theta'_s \cos \phi'_s + \cos \theta_{inc} \cos \theta'_s) \\ \text{atan2}(\sin \theta'_s \sin \phi'_s, \cos \theta_{inc} \sin \theta'_s \cos \phi'_s + \sin \theta_{inc} \cos \theta'_s) \end{pmatrix}. \quad (D2)$$

805 The Stokes rotation matrices $\underline{L}(-\varphi_s), \underline{L}(\varphi_i)$ transform the polarization basis from relative to the scattering direction to relative to incidence direction. Fig. D1 shows the geometry for polarization basis transformation. The Stokes rotation matrix $\underline{L}(-\varphi_s)$ describes the rotation by angle φ_s , which is the angle between the plane, that is spanned by the unit vector of the scattering direction \hat{e}_{ks} and the laboratory Z-axis, and the scattering plane, which is the plane that is spanned by the unit vector of the incidence direction \hat{e}_{ki} and the unit vector of the scattering direction \hat{e}_{ks} . The Stokes rotation matrix $\underline{L}(\varphi_i)$ describes the rotation by angle φ_i , which is the angle between the plane that is spanned by the unit vector of the incidence direction and

the laboratory Z-axis, and the scattering plane. The unit vector \hat{e}_{kj} describing the incidence or scattering direction is

$$\hat{e}_{kj} = \begin{pmatrix} \sin \theta_j \cos \phi_j \\ \sin \theta_j \sin \phi_j \\ \cos \theta_j \end{pmatrix} \quad (D3)$$

810 and the unit vector of the vertical polarization \hat{e}_{vj} for the incidence direction or the scattering direction is

$$\hat{e}_{vj} = \begin{pmatrix} \cos \theta_j \cos \phi_j \\ \cos \theta_j \sin \phi_j \\ -\sin \theta_j \end{pmatrix} \quad (D4)$$

with $j = i, s$ for the incidence direction and the scattering direction, respectively. The rotation angle is

$$\varphi_j = \begin{cases} -\arccos(\hat{e}_{vj} \cdot \hat{p}_j) & , \hat{e}_{vj} \cdot \hat{n}_j \geq 0 \\ \arccos(\hat{e}_{vj} \cdot \hat{p}_j) & , \hat{e}_{vj} \cdot \hat{n}_j < 0 \end{cases} \quad (D5)$$

with the unit vector

$$815 \quad \hat{p}_j = \hat{n} \times \hat{e}_{kj} \quad (D6)$$

that is parallel to scattering plane and orthogonal to \hat{e}_{kj} . The normal vector

$$\hat{n} = \frac{\hat{e}_{ks} \times \hat{e}_{ki}}{\sin \Theta} \quad (D7)$$

is orthogonal to the scattering plane. The scattering angle Θ , which is the angle between the incidence direction and the scattering direction is

$$820 \quad \sin \Theta = |\hat{e}_{ks} \times \hat{e}_{ki}| \quad (D8)$$

In the actual implementation each matrix element $M_{ij,avo}(\theta_{inc}, \theta'_s, \phi'_s)$ of the averaged Mueller matrix is represented as a spherical harmonics series over the scattering directions θ'_s, ϕ'_s . For the calculation of the averaged scattering matrix Z_{avo} , the Mueller matrix elements $M_{ij,avo}(\theta_{inc}, \theta'_s, \phi'_s)$ in angular grid representation are used. The resulting scattering matrix elements $Z_{ij,avo}$ in angular grid representation are expanded afterwards as spherical harmonics series over the scattering directions

825 θ_s, ϕ_s .

Appendix E: Spherical harmonics expansion of the Mueller and scattering matrix elements

Each matrix element $X_{ij}(\theta_{inc}, \phi_{inc}, \theta_s, \phi_s)$ of the Mueller matrix or the scattering matrix is expanded in a spherical harmonics series over the scattering directions (θ_s, ϕ_s) .

$$X_{ij}(\theta_{inc}, \phi_{inc}, \theta_s, \phi_s) = \sum_{l=0}^{l_{max}} \sum_{m=-l}^l C_{lm}(\theta_{inc}, \phi_{inc}) Y_{lm}(\theta_s, \phi_s) \quad (E1)$$

830 with Y_{lm} the spherical harmonic function of the l -th and m -th order and with

$$C_{lm}(\theta_{inc}, \phi_{inc}) = \int_{\Omega_s} X_{ij}(\theta_{inc}, \phi_{inc}, \theta_s, \phi_s) Y_{lm}^*(\theta_s, \phi_s) d\Omega_s \quad (E2)$$

the expansion coefficients of the incidence direction $(\theta_{inc}, \phi_{inc})$. To save data space, the expansion of X_{ij} is truncated to the value l_{max} . l_{max} is defined as the lowest l for which holds, that

$$\left[\int_{\Omega_s} \left| X_{ij}(\theta_{inc}, \phi_{inc}, \theta_s, \phi_s) - \sum_{l=0}^{l_{max}} \sum_{m=-l}^l C_{lm}(\theta_{inc}, \phi_{inc}) Y_{lm}(\theta_s, \phi_s) \right|^2 d\Omega_s \right]^{\frac{1}{2}} < \varepsilon_{M11}. \quad (E3)$$

835 ε_{M11} is 0.5% of the standard deviation over the scattering directions (θ_s, ϕ_s) of the $X_{11}(\theta_{inc}, \phi_{inc})$ matrix element. For the actual calculation of the spherical harmonics the SHTns library version 2.8 (Schaeffer, 2013) and its Python interface are used.

Appendix F: ~~Rotation matrix elements~~

~~The rotation matrix elements R_{ij} are~~

~~$$R_{11} = \cos(\gamma) \cos(\beta) \cos(\alpha) - \sin(\gamma) \sin(\alpha)$$~~

840

~~$$R_{12} = \cos(\gamma) \cos(\beta) \sin(\alpha) + \sin(\gamma) \cos(\alpha)$$~~

~~$$R_{13} = -\cos(\gamma) \sin(\beta)$$~~

845

~~$$R_{21} = -\sin(\gamma) \cos(\beta) \cos(\alpha) - \cos(\gamma) \sin(\alpha)$$~~

~~$$R_{22} = -\sin(\gamma) \cos(\beta) \sin(\alpha) + \cos(\gamma) \cos(\alpha)$$~~

~~$$R_{23} = \sin(\gamma) \sin(\beta)$$~~

850

~~$$R_{31} = \sin(\beta) \cos(\alpha)$$~~

~~$$R_{32} = \sin(\beta) \sin(\alpha)$$~~

855

~~$$R_{33} = \cos(\beta)$$~~

~~with Euler angles α , β , and γ (Tsang et al., 2000).~~

References

- Adams, I. S. and Bettenhausen, M. H.: The Scattering Properties of Horizontally Aligned Snow Crystals and Crystal Approximations at Millimeter Wavelengths, *Radio Science*, 47, 2012.
- 860 Bergadá, M., Labriola, M., González, R., Palacios, M. A., Marote, D., Andrés, A., García, J. L., Pascuala, D. S., Ordóñez, L., Rodríguez, M., Ortín, M. T., Estesó, V., Martínez, J., and Klein, U.: The Ice Cloud Imager (ICI) Preliminary Design and Performance, in: 2016 14th Specialist Meeting on Microwave Radiometry and Remote Sensing of the Environment (MicroRad), pp. 27–31, 2016.
- Buehler, S. A., Jiménez, C., Evans, K. F., Eriksson, P., Rydberg, B., Heymsfield, A. J., Stubenrauch, C. J., Lohmann, U., Emde, C., John, V. O., and et al.: A Concept for a Satellite Mission to Measure Cloud Ice Water Path, Ice Particle Size, and Cloud Altitude, *Quarterly Journal of the Royal Meteorological Society*, 133, 109–128, 2007.
- 865 Buehler, S. A., Defer, E., Evans, F., Eliasson, S., Mendrok, J., Eriksson, P., Lee, C., Jiménez, C., Prigent, C., Crewell, S., and et al.: Observing Ice Clouds in the Submillimeter Spectral Range: The Cloudice Mission Proposal for Esa’s Earth Explorer 8, *Atmos. Meas. Tech.*, 5, 1529–1549, 2012.
- Buehler, S. A., Mendrok, J., Eriksson, P., Perrin, A., Larsson, R., and Lemke, O.: Arts, the Atmospheric Radiative Transfer Simulator – 870 Version 2.2, the Planetary Toolbox Edition, *Geoscientific Model Development*, 11, 1537–1556, 2018.
- Côté, J., Gravel, S., Méthot, A., Patoine, A., Roch, M., and Staniforth, A.: The Operational CMC-MRB Global Environmental Multiscale (GEM) Model. Part I: Design Considerations and Formulation, *Monthly Weather Review*, 126, 1373–1395, 1998.
- Defer, E., Galligani, V. S., Prigent, C., and Jimenez, C.: First Observations of Polarized Scattering Over Ice Clouds at Close-to-millimeter Wavelengths (157 GHz) with MADRAS on Board the Megha-Tropiques Mission, *Journal of Geophysical Research: Atmospheres*, 119, 875 2014JD022 353, 2014.
- Ding, J., Bi, L., Yang, P., Kattawar, G. W., Weng, F., Liu, Q., and Greenwald, T.: Single-scattering Properties of Ice Particles in the Microwave Regime: Temperature Effect on the Ice Refractive Index with Implications in Remote Sensing, *Journal of Quantitative Spectroscopy and Radiative Transfer*, 190, 26–37, 2017.
- Draine, B. T. and Flatau, P. J.: Discrete-dipole Approximation for Scattering Calculations, *J. Opt. Soc. Am. A*, 11, 1491–1499, 1994.
- 880 Emde, C.: A Polarized Discrete Ordinate Scattering Model for Simulations of Limb and Nadir Long-wave Measurements in 1-D/3-D Spherical Atmospheres, *Journal of Geophysical Research*, 109, 2004.
- Eriksson, P., Buehler, S., Davis, C., Emde, C., and Lemke, O.: Arts, the Atmospheric Radiative Transfer Simulator, Version 2, *Journal of Quantitative Spectroscopy and Radiative Transfer*, 112, 1551–1558, 2011.
- Eriksson, P., Ekelund, R., Mendrok, J., Brath, M., Lemke, O., and Buehler, S. A.: A General Database of Hydrometeor Single Scattering 885 Properties at Microwave and Sub-millimetre Wavelengths, *Earth System Science Data*, 10, 1301–1326, 2018.
- Eriksson, P., Rydberg, B., Mattioli, V., Thoss, A., Accadia, C., Klein, U., and Buehler, S. A.: Towards an Operational Ice Cloud Imager (ICI) Retrieval Product, *Atmospheric Measurement Techniques*, 13, 53–71, 2020.
- Gong, J. and Wu, D. L.: Microphysical Properties of Frozen Particles Inferred from Global Precipitation Measurement (gpm) Microwave Imager (gmi) Polarimetric Measurements, *Atmospheric Chemistry and Physics*, 17, 2741–2757, 2017.
- 890 Hong, G., Yang, P., Baum, B. A., Heymsfield, A. J., Weng, F., Liu, Q., Heygster, G., and Buehler, S. A.: Scattering Database in the Millimeter and Submillimeter Wave Range of 100–1000 GHz for Nonspherical Ice Particles, *Journal of Geophysical Research: Atmospheres* (1984–2012), 114, 2009.

- Hou, A. Y., Kakar, R. K., Neeck, S., Azarbarzin, A. A., Kummerow, C. D., Kojima, M., Oki, R., Nakamura, K., and Iguchi, T.: The Global Precipitation Measurement Mission, *Bulletin of the American Meteorological Society*, 95, 701–722, 2013.
- 895 Khvorostyanov, V. I. and Curry, J. A.: *Thermodynamics, Kinetics, and Microphysics of Clouds*, Cambridge University Press, 2014.
- Klett, J. D.: Orientation Model for Particles in Turbulence, *Journal of the Atmospheric Sciences*, 52, 2276–2285, 1995.
- Liu, G.: A Database of Microwave Single-scattering Properties for Nonspherical Ice Particles, *Bulletin of the American Meteorological Society*, 89, 1563–1570, 2008.
- Lu, Y., Jiang, Z., Aydin, K., Verlinde, J., Clothiaux, E. E., and Botta, G.: A Polarimetric Scattering Database for Non-spherical Ice Particles
900 at Microwave Wavelengths, *Atmospheric Measurement Techniques*, 9, 5119–5134, 2016.
- Mätzler, C.: *Thermal Microwave Radiation: Applications for Remote Sensing*, vol. 52, Iet, 2006.
- Milbrandt, J. A. and Yau, M. K.: A Multimoment Bulk Microphysics Parameterization. Part I: Analysis of the Role of the Spectral Shape Parameter, *Journal of the Atmospheric Sciences*, 62, 3051–3064, 2005a.
- Milbrandt, J. A. and Yau, M. K.: A Multimoment Bulk Microphysics Parameterization. Part II: A Proposed Three-Moment Closure and
905 Scheme Description, *Journal of the Atmospheric Sciences*, 62, 3065–3081, 2005b.
- Mishchenko, M. I. and Yurkin, M. A.: On the Concept of Random Orientation in Far-field Electromagnetic Scattering by Nonspherical Particles, *Optics letters*, 42, 494–497, 2017.
- Mishchenko, M. I., Hovenier, J. W., and Travis, L. D., eds.: *Light Scattering by Nonspherical Particles*, Academic Press, 2000.
- Mishchenko, M. I., Travis, L. D., and Lacis, A. A.: *Scattering, Absorption, and Emission of Light by Small Particles*, Cambridge university
910 press, 2002.
- Mlawer, E. J., Payne, V. H., Moncet, J.-L., Delamere, J. S., Alvarado, M. J., and Tobin, D. C.: Development and Recent Evaluation of the Mt_ckd Model of Continuum Absorption, *Philosophical Transactions of the Royal Society A: Mathematical, Physical and Engineering Sciences*, 370, 2520–2556, 2012.
- Prigent, C., Aires, F., Wang, D., Fox, S., and Harlow, C.: Sea-surface Emissivity Parametrization from Microwaves to Millimetre Waves,
915 *Quarterly Journal of the Royal Meteorological Society*, 143, 596–605, 2017.
- Rosenkranz, P. W.: Water Vapor Microwave Continuum Absorption: A Comparison of Measurements and Models, *Radio Science*, 33, 919–928, 1998.
- Rothman, L., Gordon, I., Babikov, Y., Barbe, A., Chris Benner, D., Bernath, P., Birk, M., Bizzocchi, L., Boudon, V., Brown, L., and et al.: The Hitran2012 Molecular Spectroscopic Database, *Journal of Quantitative Spectroscopy and Radiative Transfer*, 130, 4–50, 2013.
- 920 Satoh, M.: *Icosahedral Grids in Atmospheric Circulation Dynamics and General Circulation Models*, Springer Praxis Books, Springer Berlin Heidelberg, 2014.
- Schaeffer, N.: Efficient Spherical Harmonic Transforms Aimed at Pseudospectral Numerical Simulations, *Geochemistry, Geophysics, Geosystems*, 14, 751–758, 2013.
- Shivakumar, S. K. and Pircher, M.: Announcement to Megha-Tropiques Science Data Users, official communiqué, 2013.
- 925 Tretyakov, M. Y., Koshelev, M. A., Dorovskikh, V. V., Makarov, D. S., and Rosenkranz, P. W.: 60-GHz Oxygen Band: Precise Broadening and Central Frequencies of Fine-structure Lines, Absolute Absorption Profile at Atmospheric Pressure, and Revision of Mixing Coefficients, *Journal of Molecular Spectroscopy*, 231, 1–14, 2005.
- Tsang, L., Kong, J. A., and Ding, K.-H.: *Scattering of Electromagnetic Waves, Theories and Applications*, vol. 27, John Wiley & Sons, 2000.
- van de Hulst, H. C.: *Light Scattering by Small Particles*, Courier Corporation, 1981.

930 Yurkin, M. A. and Hoekstra, A. G.: The Discrete-dipole-approximation Code ADDA: Capabilities and Known Limitations, *Journal of Quantitative Spectroscopy and Radiative Transfer*, 112, 2234–2247, 2011.

Zeng, X., Skofronick-Jackson, G., Tian, L., Emory, A. E., Olson, W. S., and Kroodsma, R. A.: Analysis of the Global Microwave Polarization Data of Clouds, *Journal of Climate*, 32, 3–13, 2019.